Identification and characterization of current sheets in collisionless plasmas turbulence

Amirhassan Chatraee Azizabadi

Master Thesis

Department of Physics
Freie Universität Berlin
Germany
July 2020

Supervisors:

Dr. Neeraj Jain

Prof.Dr. Jörg Büchner

Prof.Dr. Wolf-Christian Müller

Abstract

In collisionless space and astrophysical plasmas dissipation of macroscopic energy into heat in the absence of collisions is a major unsolved problem. Most plausible mechanism for the dissipation in collisioneless plasma is the turbulent cascade of energy from macroscopic scales to kinetic scales where plasma processes can dissipates the energy. Space observations alongside with computer simulations show that kinetic scale current sheets self-consistently formed in the turbulent are the sites of the energy dissipation. Kinetic processes in current sheets such as magnetic reconnection, Fermi acceleration and Landau and cyclotron damping by waves considered to be the cause of energy dissipation are directly or indirectly influenced by plasma instabilities which depend on free energy sources, structures and physical parameters of current sheets. The the objective in this research work is identification and characterization of current sheets formed in collisionless plasma turbulence. We develop a computer program in python language implementing an algorithm for identification of current sheets in the turbulence. The algorithm was developed and used by [Zhdankin et al., The Astrophysical Journal, 771:124, 2013] to identify and characterize current sheets in Magnetohydrodynamic turbulence. We validate the newly developed python program against test data generated by mathematical formula. We then apply the program to the turbulence data generated by hybrid simulations of collsionless plasma turbulence to identify and characterize current sheets formed therein. The algorithm has three parameters to be chosen. The simulation data is chosen at times when current sheets have formed but not become unstable. We characterize current sheets by first choosing appropriate values of the three algorithm parameters, viz., a threshold to get rid of background fluctuations, size of the local region around current sheet peaks and value of current density at the current sheet boundary. Robustness of the results is checked against small variation of the algorithm parameters. Current sheets are characterized in terms of peak current density, half-thickness, length and aspect ratio. Results show that current sheet thins down to grid scale have tendency to become thinner if allowed by reducing the grid spacing in the simulations. Peak current density in current sheets enhances with thinning. Current sheets have lengths several tens times larger than their thicknesses and thus a large aspect ratio (length/thickness). Implication of the characterization results for plasma instabilities in current sheets are discussed. In the last part of this research work we have presented the results of identification and characterization of current sheets from statistical point of view and compared it with theoretical aspect of plasma instabilities and discussed about the probability occurrence of these instabilities.

Acknowledgement

First I want to thank my supervisors, Dr.Neeraj Jain for all his guidance and careful reading and advising of manuscript and constructive suggestions concerning its improvement and deepest gratitude to Professor Jörg Büchner for his kindness and patience while working with me during this one year. My greatest appreciation to Professor Wolf-Christian Müller who introduced me to the SMART group and Professor Jörg Büchner for doing my master thesis and his guidance.
Finally, special thanks to my brother Dr.Shahabedin Chatraee, who has always motivated me on science and for his dedication during my education in Germany.

Amirhassan Chatraee Azizabadi, June 16th, 2020

Contents

Chapter 1

Introduction

1.1 What are plasmas?

Plasmas, known as the fourth state of matter, are collection of charged particles satisfying certain conditions. Plasmas are quasi-neutral at length scales larger than the Debye length (λ_d), an e-folding distance in which the electric potential of a charged particle in a plasma is shielded by the oppositely charged particles in thermal motions.

$$\lambda_D = \sqrt{\frac{\epsilon_0 K T_e}{n e^2}} \tag{1.1}$$

Where ϵ_0 is the electrical field constant, k_B is the Boltzmann constant, T_e or T_i is the electron or ion temperature, n is the particle density and e is the electron charge density. In other words Debye length is a distance at which the thermal energy of particles is equal to the electrostatic potential energy. The picture of Debye shielding is statistically meaningful if there are enough particles in the Debye sphere of radius λ_d. Therefore number of particles in the Debye sphere:

$$N_D = n\frac{4}{3}\pi\lambda_D^3 = 1.38 \times 10^6 T_e^{3/2}/n^{1/2} >> 1 \tag{1.2}$$

Another condition for an ionized gas to be considered as plasma is the collective behaviour: Interaction among plasma particles is dominated by long range electromagnetic forces. Collective behaviour is an essential feature of plasmas distinguishing them from other ionized gases dominated by short range near neighbour interactions among the constituent particles. An ionized gas is not considered as plasma if interactions among particles are dominated by collisions. In the case of frequent collisions, hydrodynamic forces rather than electromagnetic forces control the dynamics. Therefore product of the frequency of interest , ω, and the meantime τ between collision

with the neutral atoms should be larger than unity ($\omega\tau >> 1$) for the gas to behave like a plasma.

Plasma is the most commonly found state of matter in the universe. It is found in ionosphere and magnetoshpere of Earth, the interplanetary space in our solar system, Sun's atmosphere and interior, star interiors and accretion disk around them, and interstellar and intergalactic media. Most space and astrophysical plasmas are collisionless, i.e., mean free path for Coulomb collision is larger than the system size. For example, mean free path of Coulomb collisions in solar wind at near earth distances is of the order of the Earth-Sun distance. Warm phase plasma in interstellar medium is an example of weakly collisional plasmas: Mean free path$\sim 10^{12}$cm is much smaller than the system size $\sim 10^{20}$cm but larger than the ion gyro-radius $\sim 10^{9}$cm. These collisionless or weakly collisonal plasmas have very high Reynold's number and are, therefore, observed to be in turbulent state.

1.2 Collisionless dissipation in plasmas

Dissipation of macroscopic energy into heat in the rarity of collisions in space and astrophysical plasmas is a major unsolved problem. In collisionless plasmas, the dissipation scale due to collisions is very small compared to the energy containing macroscopic scales, and thus macroscopic energy can not be dissipated into heat by collisions. Heating of collisionless plasmas is, nevertheless, quite common phenomena in space and astrophysics. For example, spacecraft observations of solar wind show the non-adiabatic dependence of its temperature on the distance from the surface of the sun. This phenomena indicates that a separate heating mechanism, which can not be accounted for merely by collisions, is operating inside the cluster of ionized particles departed from sun. Research carried out so far using theory, numerical computation and the satellite observations strongly suggest a crucial role of plasma turbulence in the heating. Turbulence in collisionless plasmas transfer energy from macro- to micro-scales associated with electrons and ions (their inertial length and gyro-radii) constituting the plasma. Collisionless plasma processes at the kinetic scales can, then, dissipate the energy. These processes are, however, not well understood yet.

Symbol	SW	(upper) corona	Definition
$n_p \sim n_e$	5 cm^{-3}	10^6 cm^{-3}	proton and electron number density
$T_p \sim T_e$	10^5 K	10^6 K	proton and electron temperature
B_0	10^{-4} G	1 G	magnetic field strength
$v_{th,p}$	40 km/s	130 km/s	proton thermal speed
$v_{th,e}$	1700 km/s	5000 km/s	electron thermal speed
v_A	100 km/s	2000 km/s	proton Alfvén speed
Ω_p	1 s^{-1}	10^4 s^{-1}	proton gyration frequency
Ω_e	1836 s^{-1}	2×10^7 s^{-1}	electron gyration frequency
ω_p	3000 s^{-1}	10^6 s^{-1}	proton plasma frequency
ω_e	10^5 s^{-1}	6×10^7 s^{-1}	electron plasma frequency
ν_c	4×10^{-7} s^{-1}	0.5 s^{-1}	proton collision frequency
ℓ_p	100 km	300 m	proton inertial length
ℓ_e	3 km	5 m	electron inertial length
$\lambda_p \sim \lambda_e$	10 m	7 cm	proton and electron Debye length
r_p	40 km	13 m	proton gyration radius
r_e	1 km	25 cm	electron gyration radius
$\lambda_{mfp,p}$	10^8 km	250 km	proton collisional mean free path
$\beta_p \sim \beta_e$	0.2	0.003	proton and electron beta

Table 1:Parameters in solar wind (SW) at 1 AU and solar corona. Value are taken from [1, 2]

1.3 Collisionless plasma turbulence

1.3.1 Power spectrum: solar wind

Distribution of energy transferred from large to kinetic scales by plasma turbulence is well represented by Fourier power spectrum. Figure 1.1 shows power spectrum of magnetic field with frequency as observed by Cluster spacecraft at 1 AU in solar wind which provides an excellent laboratory to study collisionless plasma turbulence[3]. Table 1 list the typical solar wind parameters. The spectrum can be divided in three frequency ranges separated by two breaks in the spectrum.

The location of these breaks are related to the characteristic ion and electron scale [Figure 1.1]. But determination of exact locations of these breaks is still under active research[4]. In the first range of frequencies smaller than the ion cyclotron frequency, $f < f_{ci}$, power spectrum exhibits a power law with a spectral index 1.7 close to the spectral index of the Kolmogorov power law for fluid turbulence . In the second frequency range $f_{ci} < f < f_{\lambda e}$, the power spectrum becomes steeper with a spectral index of 2.8 forming a break in the spectrum at f_{ci}. In the third frequency range, $f > f_{\lambda_e}$, the power spectrum steepens further forming a second break at $f \sim f_{\lambda e}$.

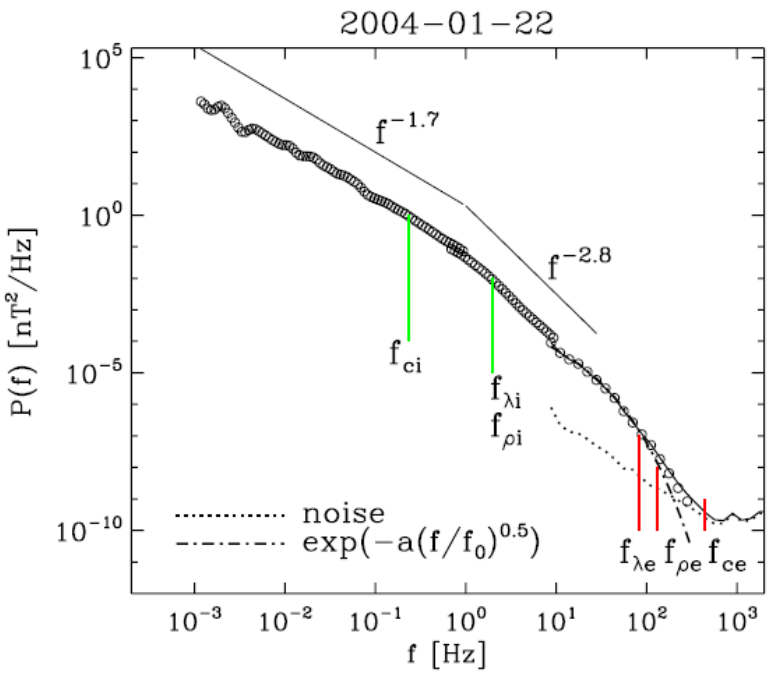

Figure 1.1: Adopted from Alexandrova et all (2009)[3]. Magnetic power spectrum from solar wind at 1 AU. Here f_c denotes the frequency of gyration and f_ρ and f_λ indicate the frequency of thermal and inertial length respectively.[3]

1.3.2 Magnetohydrodynamic turbulence

At large scales, $f < f_{ci}$, magnetohydrodynamic (MHD) model of plasma is applicable. Kraichnan and Iroshnikov extended Kolmogorov's hypothesis of fluid turbulence to plasmas and were the first to propose a phenomenological model of incompressible MHD turbulence [5]. Kolmogorov's hypothesis assert that the rate of nonlinear energy transfer is constant at all scales in the inertial range. At a given scale the energy transfer is spectrally local with rates determined by the turbulent condition at that scale. Kraichnan and Iroshnikov proposed that magnetic field of large scale fluctuations acts as the mean field[6]. Assuming isotropy and taking into account weak nonlinear interactions of Alfven wave packets moving towards each other along the mean magnetic field, Kraichnan and Iroshnikov predicted an inertial range wave-number spectrum scaling as $k^{-3/2}$.

Numerical simulations and solar wind observations, however, revealed that the power spectrum of magnetic field is not isotropic as assumed by Kraichnan and Iroshnikov[7–9]. In strong MHD turbulence, Goldreich and Sridhar proposed a critical balance between the time of nonlinear interactions perpendicular to the mean magnetic field and the time of linear propagation parallel to the mean magnetic field [10]. They predicted a Kolmogorov-like magnetic field spectrum scaling as $k_\perp^{-5/3}$ and a scale dependent anisotropy $k_{||} \propto (k_\perp)^{2/3}$. Most solar wind observations, e.g., the one in Figure 1.1, seems to favor the Goldreich-Sridhar scaling of magnetic field spectra. Numerical MHD simulations of strongly magnetized turbulence, however, shows $k^{-3/2}$ scaling

[11, 12]. Dynamic alignment of the polarization of the magnetic- and velocity-field fluctuations was proposed to explain the $k^{-3/2}$ scaling in the numerical simulations [13].

1.3.3 Kinetic turbulence and current sheets

Ion kinetic physics becomes important, invalidating MHD model, for frequencies of the order of or larger than the ion cyclotron frequency about which magnetic field power spectrum steepens producing a spectral break (Figure 1.1). At these scales, a variety of kinetic plasma processes can play roles in the dynamics of turbulence. Numerical simulations suggest that current sheets are formed at ion kinetic scales in plasma turbulence and co-exist with or are manifestation of kinetic plasma waves [14]. Thicknesses of these current sheets range from ion to electron scales unlike the Kolmogorov scale current sheets formed in MHD simulations [15]. Spacecraft observations in solar wind and Eath's magnetosphere also reveal existence of current sheets in plasma turbulence [16]. Numerical simulations and spacecraft observations have further shown that a large part of the dissipation of the fluctuations and plasma heating occur in and around the current sheets [15, 16]. The kinetic plasma processes responsible for the dissipation and heating in the current sheets are, however, not well understood.

Several kinetic plasma processes in current sheets have been proposed to cause collisionless dissipation and heating in plasma turbulence. Magnetic reconnection in current sheets of plasma turbulence is one of the possible processes which can dissipate the turbulent fluctuations. It generates parallel electric fields which can accelerate the charged particles [17]. Further, magnetic islands of varying size form and evolve in magnetic reconnection. Charge particles trapped inside contracting magnetic islands [18] can be accelerated by Fermi-like processes. Stochastic ion heating [19], and Landau and cyclotron damping [20] in current sheets have also been considered for collisionless dissipation.

1.4 Plasma instabilities in current sheets of turbulence

The kinetic plasma processes responsible for the dissipation in kinetic scale current sheets can be, directly or indirectly, influenced by plasma instabilities. For example, magnetic reconnection in current sheets formed in plasma turbulence is basically a tearing instability. Plasma instabilities in current sheets can generate large amplitude plasma waves which can lead to the stochastic ion heating [21]. Plasma instabilities

can generate their own turbulence affecting the properties of the encompassing turbulence and providing anomalous dissipation

Growth of plasma instabilities in current sheets and their nonlinear consequences for the dissipation depend upon free energy sources available in current sheets of turbulence as well as on physical parameters and structure of the current sheets. Free energy sources can arise either from spatial gradients of macroscopic variables (density, velocity and pressure) and/or by non-Maxwellian features of plasma particles' distribution functions. Examples of plasma instabilities driven by spatial gradients are tearing, lower-hybrid drift, drift kink, drift sausage and Kelvin-Helmholtz instabilties and those driven by non-Maxwellean distribution function are ion cyclotron, firehose, mirror and bump-on-tail instabilities. Both type of instabilities can grow and mutually interact in current sheets [22–24]. For example tearing instability of an ion-scale current sheet can be enhanced by ion cyclotron instability while suppressed by firehose instability [25].
It is not known yet which out of many possible plasma instabilties grow in current sheets of turbulence and how they affect the dissipation. Growth of plasma instabilities in current sheets and their nonlinear consequences for the dissipation depend upon free energy sources available in current sheets as well as on physical parameters and structure of the current sheets. Therefore current sheets forming in plasma turbulence need to be characterized in terms of free energy sources, physical parameters and structure to understand the role of plasma instabilities in collisionless dissipation.

1.5 Goal of this thesis

The over-all goal of this thesis is to characterize the current sheets self-consistently formed in collisionless plasma turbulence in terms of their physical structure, parameters and free energy sources. For this purpose, we first developed a computer Python program to first identify and then characterize the current sheets in turbulence. We implemented an algorithm of current sheet identification and characterization used previously by Zhdankin et al. (2013) [26] to characterize the current sheets formed in MHD simulations of plasma turbulence. In the study phase of this thesis, we have implemented the current sheet identication part of the algorithm in the computer program. The implementation of current sheet characterization part of the algorithm was carried out in the research phase. We then applied our newly developed computer program employing the algorithm of Zhdankin et al. (2013) [26] to characterize the current sheets in PIC-hybrid simulations of collisionless plasma turbulence. Before applying the program to the hybrid simulations, it was validated against test data which is gen-

erated not by the simulations but by mathematical functions.

1.6 Thesis organization

This thesis is organized in five chapters outlined below. The first chapter is introduction of the subject matter of this thesis. In this chapter we discuss some basic of plasmas properties, and discuss about the turbulence in space and astrophysical plasmas and the role of current sheets and plasma instabilities in collisionless plasma turbulence to motivate our work in this thesis. The second chapter discusses hybrid simulation model of plasmas implemented in the numerical code AIKEF which is used to produce the turbulent current sheet data. This data will also be presented in the second chapter. In the third chapter we have introduced the algorithm for identification and characterization of current sheets in the plasma turbulence following Zhdankin et al. (2013) [26] and a method of the generation of test data to be used for authentication and validation of our algorithm before implementation on the hybrid simulation. In this chapter we validate our python based computer program against the test data and show how results depends on the different parameters.

In the forth chapter we present the results obtained by application of our python program to the hybrid simulation data. The last but not the least, in the chapter 5 we conclude the thesis work by discussing the implications of our results for plasma instabilities in current sheets formed in collisionless plasma turbulence and future directions of our work.

Chapter 2

Hybrid simulation of collisionless plasmas turbulence

2.1 Hybrid plasma model

In this chapter we discuss the hybrid model of plasmas and results obtained by hybrid simulations of collisionless plasma turbulence. There are several methods to simulate plasmas such as the fluid and fully kinetic plasma model but the properties of hybrid model makes it singular for the study of turbulence in collisionless plasma at ion kinetic scale. Specially when we need a model to describe a phenomena that occurs on the short space and time scale which can not be treated by magneto hydrodynamics (MHD) and yet do not resolve the processes that occur on the electron scale. The appropriate scales are ion gyro-radius and ion inertial spatial scale and inverse ion gyro frequency time scale [27]. In the case of space plasmas these length scales are tens to hundreds of km and times on the order of second. Unlike the fully kinetic plasma model which describes the motion of ions and electrons kinetically, hybrid model describes electron with the fluid theory and ions with the kinetic theory.

2.1.1 Equation and approximation

Equations of hybrid plasma model can be obtained from the full set of vacuum Maxwell's equations for electromagnetic field and Vlasov equation for plasma particle. The full set of equations is displayed below. Maxwell equations for electric field E and magnetic field B:

$$\nabla.\vec{B} = 0 \tag{2.1}$$

$$\nabla.\vec{E} = \frac{\rho}{\epsilon_0} \tag{2.2}$$

$$\nabla \times \vec{B} = \frac{1}{c^2}\partial_t \vec{E} + \mu_0 \vec{j} \tag{2.3}$$

$$\nabla \times \vec{E} = -\partial_t \vec{B} \tag{2.4}$$

Where physical constants (μ_0, ϵ_0 and c) have their usual meaning and the Vlasov equation for the s-th particle species:

$$\partial_t f_s + \vec{v}.\partial_x f_s + \frac{q_s}{m_s}[(\vec{E} + \vec{v} \times \vec{B}).\partial_v f_s] = 0 \tag{2.5}$$

Here the f_s, q_s and m_s denote distribution function, charge and the mass of the s-th particles species, respectively. We will use subscript 'e' for electrons and 'i' for ions.

Vlasov equations for particle species are coupled to Maxwell equations by charge and current density, ρ and j, respectively, which can be obtained from the moments of the distribution function.

$$\rho(x) = \sum_s q_s \int f_s(\vec{x}, \vec{v}) d^3\vec{v} \tag{2.6}$$

$$\vec{j} = \sum_s q_s \int \vec{v} f_s(\vec{x}, \vec{v}) d^3\vec{v} \tag{2.7}$$

The ion space and time scales, of interest for the hybrid description of plasmas, allow to make certain approximations in the full set of equations. The advantage is that the reduced set of equations is computationally less demanding. Quasi-neutrality approximation of plasmas valid for frequencies ω much smaller than electron plasma frequency ω_{pe} and scale lengths L larger than Debye length λ_D is made as ω and L satisfy,

$$\omega \sim \omega_{ci} << \omega_{pe} = \sqrt{\frac{e^2 n_e}{\epsilon_0 m_e}} \tag{2.8}$$

$$L \sim \rho_i, d_i \gg \lambda_D = \sqrt{\frac{\epsilon_0 k_B T_e}{e^2 n_e}} \tag{2.9}$$

where ρ_i, d_i and ω_{ci} are the gyro-radius, inertial length and gyro-frequency of ions, respectively. Other symbols denote electron number density (n_e), electron temperature (T_e), electronic charge (e) and Boltzmann constant (k_B). Displacement current in Eq. (2.3) is neglected for ion space and time scales. This gives,

$$\nabla \times \vec{B} = \mu_0 \vec{j} \tag{2.10}$$

Since ion space and time scales are larger than the corresponding electron scales, electrons remain magnetized for $\omega \sim \omega_{ci}$ and $L \sim \rho_i$. Therefore the description of electrons can be approximated by fluid equations which are obtained by taking velocity moment of the Vlasov equation for electrons. Zeroth and first velocity moment of the Vlasov equation give mass and momentum conservation equations displayed below, respectively.

$$\frac{\partial \rho_e}{\partial t} + \nabla.(\rho_e \vec{u_e}) = 0 \tag{2.11}$$

$$\frac{d}{dt}(n_e m_e \vec{u_e}) = -e n_e (\vec{E} + \vec{u_e} \times \vec{B}) - \nabla P_e + e n_e \eta . \vec{j} \tag{2.12}$$

where electron density n_e, electron bulk velocity u_e and electron pressure p_e are obtained from the first three velocity moments of the electron distribution function and η is the plasma resistivity. In quasi-neutral hybrid model, electron mass conservation equation is not needed because electron number density can be obtained from the quasi-neutral condition, $n_e = n_i$, where n_i is the ion number density calculated from zero-th moment of the ion's distribution function. Replace

An often made approximation in hybrid plasma models is to consider electrons mass-less by taking limit of $m_e = 0$ in Eq.(2.12) . There are, however hybrid plasma model with finite electrons mass to include the physical effects at electron inertial scales. But for the large scale and low frequency phenomena, considering electrons with $m_e = 0$ is an good approximation. Hence equation 2.12 becomes:

$$\vec{E} = -u_e \times \vec{B} - \frac{1}{n_e e} \nabla P + \eta \vec{j} \tag{2.13}$$

An advantage of mass-less electrons is that electric field can be directly calculated from Eq. (2.13) without solving a differential equation. The disadvantage is that the requirement of small time step to satisfy Courant condition becomes severe because

propagation velocity of whistler waves increases boundlessly with wave number in the limit of mass-less electrons. A work around the avoid smaller time step is to choose a articial value of resistivity so that whistlers are damped at grid scales.

Using the quasi-neutrality condition $n_i = n_e = n$ and Ampere's law $\nabla \times \vec{B} = \mu_0 ne(\vec{u}_i - \vec{u}_e)$ to eliminate $\vec{u}_e$, the electric field is:

$$E(\vec{u}_i, \rho, \vec{B}, P_e) = -\vec{u}_i \times \vec{B} + \frac{\nabla \times \vec{B} \times \vec{B}}{\mu_0 \rho} - \frac{\nabla p}{\rho} + \eta \frac{\nabla \times \vec{B}}{\mu_0} \tag{2.14}$$

Eq.(2.14) is called Generalized ohm's law. With this equation the electric field E can be obtained only from moments of ion distribution function u_i and ne as well as B . An adiabatic law is used for electron pressure p_e.

$$\frac{p_e}{n_e^k} = constant \tag{2.15}$$

Where k is the adiabatic constant.

By combination of eq 2.14 and Faraday's law we can obtain an equation for magnetic field.

$$\partial_t \vec{B} = \nabla \times \left(\vec{u}_i \times \vec{B}\right) - \nabla \times \left(\frac{\nabla \times \vec{B} \times \vec{B}}{\mu_0 \rho_c}\right) - \eta \nabla \times \left(\frac{\nabla \times \vec{B}}{\mu_0}\right) \tag{2.16}$$

In the right hand side of equation 2.16, each term describes an important concept. The first term which is called 'convection' describes the convection of magnetic field due to the plasma flow $\vec{u}_i$. The second term is 'Hall ' term and describes the electric field which arises from current $\vec{j}$ because of Hall effect. The third term is 'resistive' term which includes the anomalous resistivity effect in eq 2.14 and leads to dissipation of magnetic field in eq 2.16.

In hybrid plasma model ions are treated kinetically By solving either Vlasov equation for distribution function f_s for ion species s or equations of motion for individual particles by particle-in-cell (PIC) method. Both approaches have their advantages and disadvantages. The Vlasov approach is computationally more expensive than the PIC approach but does not have the problem of numerical noise inherent in PIC approach. Code AIKEF used for turbulence data generation in this thesis solves the equations of motion,

$$\frac{d\vec{v}_p}{dt} = \frac{q_p}{m_p}(\vec{E} - \eta \frac{\nabla \times \vec{B}}{\mu_0} + \vec{v}_p \times \vec{B}) \tag{2.17}$$

$$\frac{dx_p}{dt} = \vec{v}_p \tag{2.18}$$

Here x_p, v_p, q_p and m_p denotes the individual position, velocity, charge and mass of distinguished particle respectively. The index p runs over all particles and resistive term in the eq 2.17 is canceled with the corresponding terms in eq 2.14 due to the conservation of overall momentum of system. The current and charge densities $\vec{j}$ and ρ are calculated from individual particle's position and velocity using particle shape functions for all ion species and u_i can be obtained by $\vec{u}_i = \vec{j}/\rho$.

Normalized equations

In numerical codes physical quantities in equations to be solved are usually normalized to the certain background values. The reason is to eliminate the natural constant such as μ_0 and to avoid round off error. The normalized physical quantities can be written as,

$$A^* = \frac{A}{A_0} \tag{2.19}$$

Here A, A_0 and A^* are physical constant, the normalisation value and the resulting dimensionless quantity, respectively.

Quantity	A	A_0	Numerical value
Magnetic eld strength	B	B_0	5nT
number density	n	n_0	$5cm^{-3}$
Time	t	$t_0 = \Omega_{i0}^{-1}$	$2s$
Length	x	$x_0 = c/\omega_{p,i0} = v_{A_0}\Omega_{i0}^{-1}$	$85km$
Velocity	v	$v_0 = x_0/t0 = v_{A_0}$	$48km/s$
Mass density	ρ_m	$\rho_{m_0} = m_p n_0$	$8.4 \times 10^{-3} \mu g km^{-3}$
Charge density	ρ_c	$\rho_{c0} = e n_0$	$8 \times 10^{-4} C km^{-3}$
Mass	m	$m_0 = \rho_{m0} x_0^3$	$5.2 \times 10^{-6} kg$
Charge	q	$q_0 = \rho_{c0} x_0^3$	$491C$
Current density	j	$J_0 = e n_0 v_{A_0}$	$3.8 \times 10^{-2} \mu A m^{-2}$
Electric field	E	$E_0 = v_0 B_0 = v_{A_0} B_0$	$0.24 mV/m$
Pressure	p	$p_0 = B_0/(2\mu_0)$	$0.01 nPa$

Table 2: Normalization constants and their typical numerical values in solar wind at 1 AU for various physical quantities [28].

Following are the equations of hybrid plasma model normalized according to the normalization scheme in Table 2.

1- Normalized Ampere's law:

$$\nabla^* \times \vec{B}^* = \vec{j}^*. \tag{2.20}$$

2- Normalized Faraday's equation:

$$\partial_{t^*} \vec{B}^* = -\nabla^* \times \vec{E}^* \tag{2.21}$$

3- Normalized Ohm's law:

$$\vec{E}^* = -\vec{u_i}^* \times \vec{B}^* + \frac{\nabla^* \times \vec{B}^* \times \vec{B}^*}{\rho} + \frac{1}{2}\frac{\nabla^* p_e^*}{\rho^*} + \eta^* \nabla^* \times \vec{B}^* \tag{2.22}$$

Here dimensionless quantity $\eta^* = \eta e n_0 / B_0$.

4- From the result of normalized Faraday's equation and Ohm's law we obtain time evolution of magnetic field:

$$\partial_{t^*} \vec{B}^* = \nabla^* \times (\vec{u_i}^* \times \vec{B}^*) - \nabla^* \times (\frac{\nabla^* \times \vec{B}^* \times \vec{B}^*}{\rho^*}) - \eta^* \nabla^* \times \nabla^* \times \vec{B}^* \tag{2.23}$$

$$\frac{p_e^*}{(n_e^*)^k} = constant \tag{2.24}$$

6- Equation of motion for ions:

$$\frac{d\vec{v}_p^*}{dt^*} = \frac{q_p^*}{m_p^*}(\vec{E}^* + \eta^* \nabla^* \times \vec{B}^* + \vec{v}_p^* \times \vec{B}^*) \tag{2.25}$$

$$\frac{d\vec{x}_p^*}{dt^*} = \vec{v}_p^* \tag{2.26}$$

2.2 Results of hybrid simulation

In this thesis, for the identification and characterization of current sheets we use the turbulence data generated by hybrid simulations of collisionless plasma turbulence using the A.I.K.E.F code (Adaptive Ion-Kinetic Electron-Fluid) from Technical University Braunschweig [29].

2.2.1 Simulation setup

Simulations initialized with random phased fluctuations of magnetic field and plasma velocity imposed on a uniform and isotropic background plasma are carried out in an x-y plane. A uniform magnetic field $B_0\hat{z}$ perpendicular to the simulation plane is applied. Initial magnetic field fluctuations are obtained from vector potential as follow:

$$\tilde{A} = \hat{z} \sum_{k_x,k_y} \delta A_z(k_x,k_y) sin(k_x x + k_y y + \phi(k_x,ky)) \tag{2.27}$$

Here k_x and k_y are wave numbers in x- and y-direction, respectively, and ϕ is the wave-number dependent random phase. We choose the amplitude δA_z of the magnetic vector potential in a way that the amplitude of magnetic field fluctuation $\delta B_\perp = \delta A_z k_\perp$ is wave number independent which means all initialized modes have the same energy. Plasma velocity fluctuations have the same form as magnetic field fluctuations except the random phases so that the magnetic and velocity fluctuations have vanishing correlation but equi-partition of energy.
The fluctuations have root mean square value of $B_{rms}/B_0 = 0.24$ and are initialized in the wave number range $|k_{x,y}d_i| < 0.2 (k_{x,y} \neq 0)$. Electron and ion plasma beta are $\beta_e = 0.5$ and $\beta_i = 0.5$, respectively. The simulation box size for the based run is $256d_i \times 256d_i$ with 512×512 grid points, 500 particles per cell and the time step $\Delta t = 0.01\Omega_{ci}^{-1}$. Simulations are also carried out by varying number of grid points, particles per cell and time step to check the effect of numerical parameters. Boundary conditions are periodic in all directions.

2.2.2 Current sheet formation and data selection

Figure 2.2 shows current density parallel to the applied magnetic field at three different times. As it can be seen (worm like structure) current sheets are formed by $\omega_{ci}t = 50$. Later these current sheets start become unstable as can be seen at gets $\omega_{ci}t = 100$ and gets signicantly disrupted by $\omega_{ci}t = 150$. As our objective in this thesis is identification and characterization of current sheets before they become unstable, we will characterize current sheets around $\omega_{ci}t = 50$ time frame. Also, RMS value of perpendicular magnetic field peaks at $\omega_{ci}t = 50$ which can be taken as an indicator of peak activity of current sheet formation, as shown in figure 2.1 .

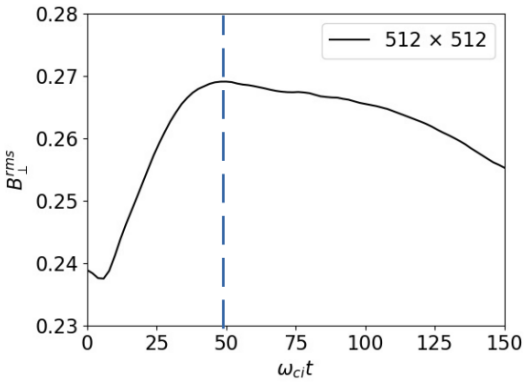

Figure 2.1: The time of peak in the evolution of $B_\perp^{rms}$ which is an indicator of peak activity of CS formation around $\omega_{ci}\,t = 50$.

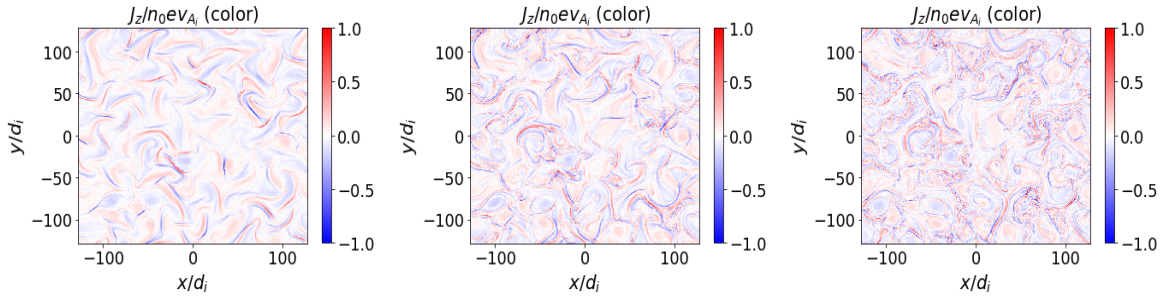

Figure 2.2: Current density J_z in $x-y$ plane ate $\omega_{ci}\,t = 50, 100$ and 150 from left to right respectively.

Evolution of current sheets make changes in their shape, geometrical features and positions even before they become unstable. So a question arises if $\omega_{ci}\,t = 50$ is an appropriate time for current sheet characterization. Figure 2.3 shows parallel current density at different times and their time average around $\omega_{ci}\,t = 50$. It can be seen in Figure 2.3 that changes in current sheets with time around $\omega_{ci}\,t = 50$ are hardly noticeable. The time average current density also looks similar to the current density at $\omega_{ci}\,t = 50$. Therefore we can use the data at $\omega_{ci}\,t = 50$ for current sheet characterization. Alternatively time average data can be used.

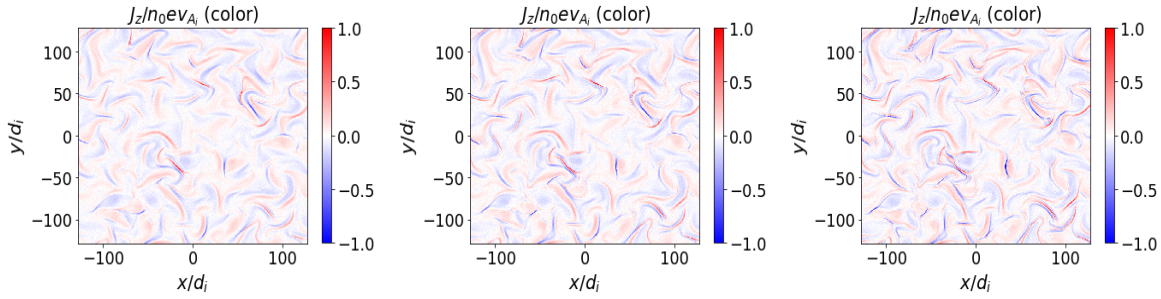

$\omega_{ci}\,t = 40$ $\omega_{ci}\,t = 50$ $\omega_{ci}\,t = 60$

Figure 2.3: Current density J_z in $x-y$ plane ate $\omega_{ci}\,t = 40, 50$ and 60 from left to right respectively.

2.2.3 A condition for current sheet identification

The algorithm of current sheet identication in turbulence, described in chapter 3, filters background fluctuations from the current density data by applying a condition. In the original Zhdankin's algorithm, this condition is a threshold on current density which could be several times the root-mean-square current density. The simulations, on the other hand, revealed that parallel electron bulk velocity u_{ez} is much larger than parallel ion bulk velocity (u_{iz}) in current sheets, which can be used as a criterion to isolate current sheets from the background turbulence.

2.2.4 Velocity distribution of particles

Another set of data that we obtained from simulation is the velocity of particles in the 2D plane frame work. These velocities are the indicator of velocity distribution among electrons and ions. Velocity distribution of particles have important information about the turbulence and instabilities in current sheets as the sites of energy dissipation. Therefore these information can be used as a condition for the characterizing current sheets in simulation of plasmas.

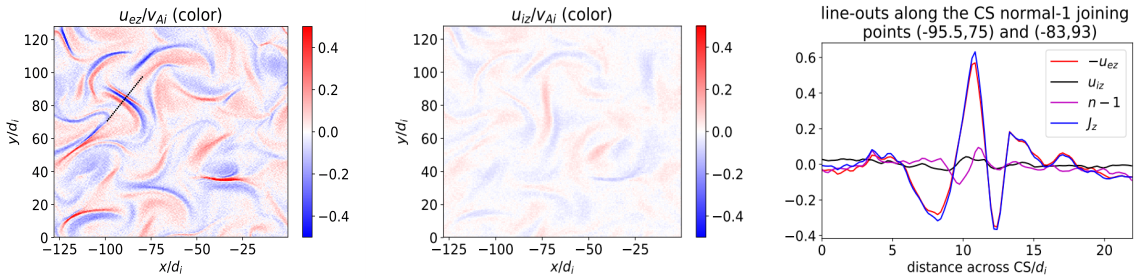

Figure 2.4: Parallel bulk velocities of electrons (left) and ions (middle) in a quarter of the simulation box and their line-outs (right) along the dashed line (a current sheet normal) shown in the left panel at $\omega_{ci}t = 50$.

Figure 2.4 shows parallel bulk velocities of electrons and ions in a quarter of simulation box. The parallel bulk velocity of electrons is much larger than the parallel bulk velocity of ions in current sheets. Line-out across a current sheet from simulations clearly shows that the parallel current density in a current sheet is dominated by electrons motion rather than ions.

Left panel in Figure 2.5 shows the ratio $|u_{ez}|/u_{iz,rms}$ at $\omega_{ci}t = 50$ in the whole simulation plane, where $u_{iz,rms}$ is the root-mean-square value of u_{iz}. It can be seen that this ratio is greater than (approximately) eight in current sheets. Setting J_z equal to zero at all the locations where $|u_{ez}|/u_{iz,rms} < 8$ and then plotting it in the right panel of Figure 2.5 shows that most of the background fluctuations are removed and mostly current sheets are visible. Therefore we can isolate current sheets from background fluctuations by using a threshold for the values of $|u_{ez}|/u_{iz,rms}$. This threshold is not same

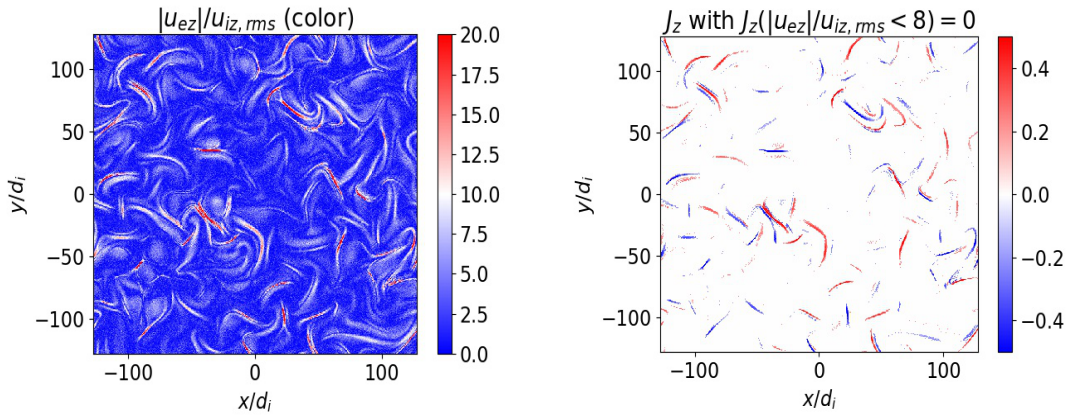

Figure 2.5: Color Plot of $|u_{ez}|/u_{iz,rms}$ (Left) J_z (right) with a mask $J_z[u_{ez}/u_{iz,rms} < 8] = 0$

for all simulations and needs to be found for each simulation by making, for example, plots like in the left panel of Figure 2.4.

2.3 Conclusion

In this chapter we have described essential of hybrid simulation of plasmas and have shown the primary physical equations lies behind this method. Also we explain briefly about the A.I.K.E.F that we used for our simulation. At the last part we showed the results of simulation from this method in different time frame and discussed about choosing appropriate time frame of simulation where current sheets are formed and stable before they start to distort and distract by the evolution of time. Additionally, we illustrated the results of electrons and ions velocity and we described that the speed motion of electrons are much larger than the speed motion of ions in current sheets which can be used as condition for current sheet characterization. In the next chapter we will introduce the algorithm of identification and characterization of current sheets in hybrid simulation of collisionless plasmas as well as new test method for referred algorithm.

Chapter 3

Algorithm of current sheet identification and characterization

The goal of this thesis is to identify and characterize the current sheets which form at kinetic scales in collisionless plasma turbulence. For this purpose we develop a computer python program implementing the algorithm of current sheet identification and characterization discussed by Zhdankin et al.(2013) [26] and refer to it as Zh -algorithm.

In this chapter we describe the Zh-algorithm [26]. We also discuss the method by which we generate the test data of "current sheets in turbulence". This test data will be used to verify the python program before its application to the actual data generated by hybrid simulations of collisionless plasma turbulence.

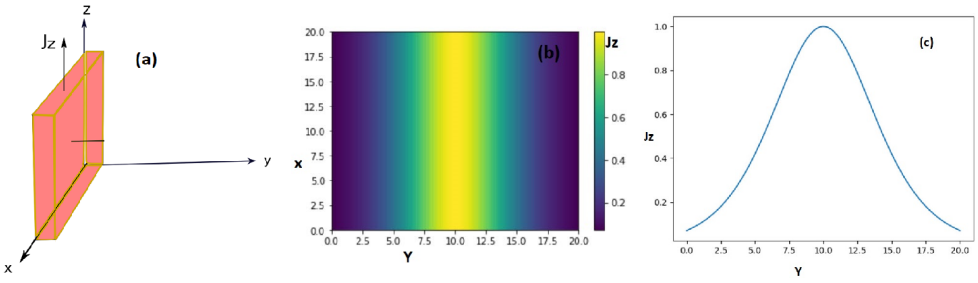

Figure 3.1: (a)Illustration of a current sheet. (b) Color plot of current density J = $sech^2$(x) in an x-y plane (c) Lineout of J across its thickness.

3.1 Current sheets

current sheet is a spatial current structure in which electric current flow is confined to a thin layer.i.e., one of the dimensions of current flow region is much smaller compared to the other two dimensions. Figure 3.1a, illustrates a laminar current sheet in which electric current flowing in the z direction is confined in the y direction but extended in

the x and z direction. Current sheets are commonly represented graphically by plotting the variation of the current density in a cross-sectional plane of the current sheet , as shown by a color plot of current density $J_z = sech^2(\frac{y}{L})$ for $L = 1$ in the $x - y$ plane in Figure 3.1.b. Current density in a current sheet peaks at the current sheet center and drops to zero on the either side of the peak in the distance of the order of L known as the half of thickness of the current sheet (Figure 3.1.c)

Figure 3.1.b shows a laminar current sheet in which current density varies smoothly. Current sheets forming in the collisionless plasma turbulence are , however not necessarily smooth. Figure 3.2 shows current density obtained from 2-D PIC-hybrid simulations of collisionless plasma turbulence. Worm like structures in the current density seen in the figure 3.2.a are current sheets with irregular shapes, random orientations and locations, finite length in the direction perpendicular to the thickness-direction, tendency of clustering and are embedded in turbulent fluctuations. Figure 3.2b shows a line out of J_z along x. Our task is to first identify such current sheets embedded in turbulent fluctuations and then characterize them.

3.2 Identification of current sheets

One of the characteristic of a current sheet is the peak current density. Thus, a natural starting step in search of current sheets is to look for local maxima in current density magnitude. But current density in plasma turbulence, as illustrated in Figure 3.1b, can have several tiny peak(due to the turbulent fluctuations) which don't qualify as current sheets. Therefore the algorithm should avoid such peaks while looking for local maxima in current density. This is achieved in Zh-algorithm by defining a threshold current density J_{th} sufficiently larger than the typical fluctuation level and selecting only the data points for which magnitude of current density is greater than the threshold value. Then we search for local maxima only at the selected points. Alternatively a threshold on the ratio of the parallel electron bulk velocity to the root-mean-square value of parallel ion bulk velocity, as discussed in chapter 2, can be used to isolate current sheets from the background uctuations.

Next step is to find local maxima. Hence, algorithm scans through all the data points where current density is above the specified J_{th} and selects those points which are local maxima in the region surrounded by n points on either side of the candidate point in each direction. Figure 3.3 shows a candidate point indexed by (i, j) surrounded by $(2n+1)^2$ points of local region in the 2-D case. The number of local maxima

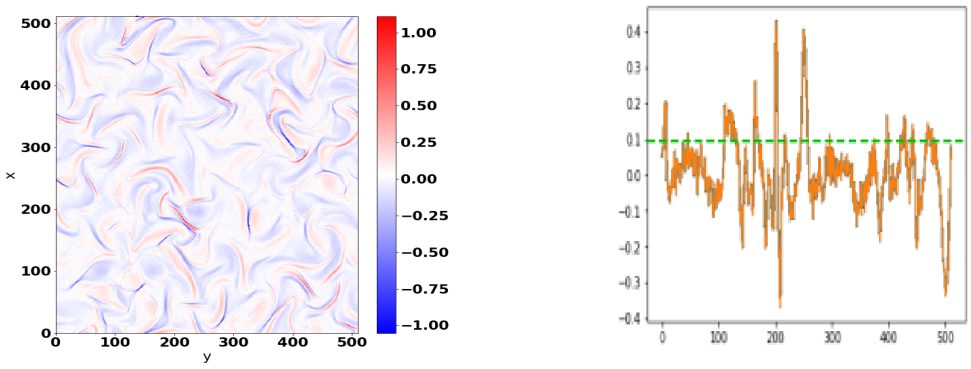

Figure 3.2: (a) Current density obtained by PIC-hybrid simulation of collisionless plasma turbulence.(b) Turbulence line-out of current density along x. Green line indicates the specified J_{th}.

found by the algorithm may depend on the choice of n. For instance by increasing n, algorithm checks for the local maxima at the candidate point in a larger local region. Therefore number of local maxima might decrease. The value of n will be chosen by experimentation so that well-resolved individual peaks can be separately identified. We associate every local maximum found by the algorithm with the peak current density of a current sheet. The location and values of the current density peaks are stored.

The next step in Zh-algorithm [26] is to identify those points which belong to each current sheet. In a smooth current sheet shown in Figure 3.1c, the current density drops from its peak value to vanishingly small values in distances of the order of half-thickness of the current sheet. Therefore points belonging to the current sheet can be defined to be the points where the current density is larger than a sufficiently small value and which are collectively connected to the point of peak current density. The condition that is defined in algorithm for identifying current sheet points is that each point has the magnitude of the current density greater than a minimal value of $J_{min,i} = J_{max,i}/2$ (i denotes the ith local maxima or current sheet).

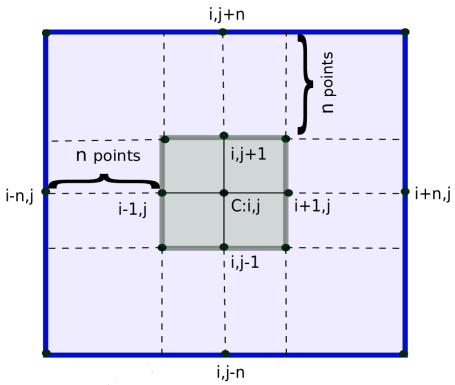

Figure 3.3: A local region surrounding a candidate point $C(i,j)$ and containing $(2n+1)^2$ points(n points on either side of point C) in $2-D$. In Zh-algorithm[26], magnitude of current density at candidate point $C(i,j)$ is checked for it to be local maximum over this local region.

The procedure to find current sheet points in algorithm is illustrated in figure 3.4. For i-th local maximum which automatically satisfies the condition $J > J_{min,i}$, the pro-

cedure starts by checking the condition at four adjacent points in 2-D (six in 3-D), located immediately above, below, left and right of the local maximum(see Figure 3.4a). Then the local maximum and the adjacent points where the condition is satisfied are added to a list of current sheet points discarding the points where the condition is not satisfied. For each new point added to the list, the algorithm checks at new set of points which are adjacent(immediately left, right, above, below) to the new point but have not been checked yet. Figure 3.4b shows that two out of the four adjacent points, shown in red in Figure 3.4a, are added (marked blue) to the list while the other two are discarded (marked green). The condition is now checked at new set of unchecked points which are marked red in Figure 3.4b and are adjacent to the newly added points. The procedure continues, as in Figure 3.4c, until no new point satisfying the condition is found.

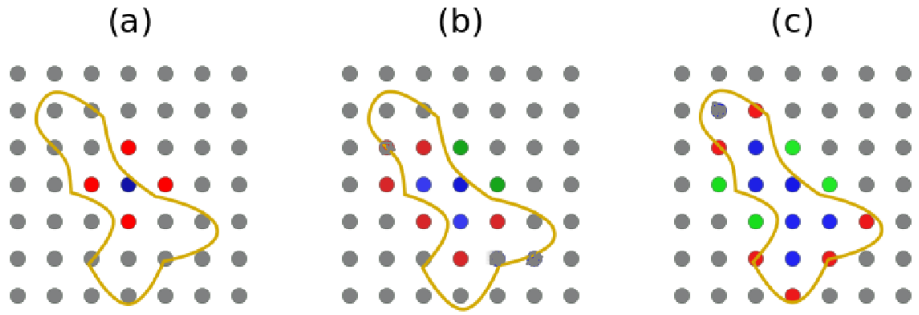

Figure 3.4: A series of steps in algorithm [26], from (a) to (c), to find points belonging to the i-th current sheet (region enclosed by closed contour) where the condition $J > J_{\{min,i\}} = J_{\{max,i\}}/2$ is satisfied. The color of a grid point (filled circles) at a given step indicates if the condition is satisfied (blue), not satisfied (green), will be checked (red) or will not be checked (gray) at that grid point. The blue point in (a) is a local maximum in current density from where the procedure starts

There is however ambiguity regarding how to treat current sheets that contains multiple peaks. If a particular current sheet has $J_{min,i} > J_{th}$, then it is possible for nearby peaks to be associated with the second current sheet that contains points shared with the first current sheet. Whether or not such a current sheet should be considered as independent is unclear.

3.3 Characterization of current sheets

The next step after identification of current sheets is to characterize the structures of current sheets. These current sheets are characterized by the thickness, length and height. The smallest dimension of the current sheet is the thickness, which is perpendicular to the length and height. Then, there is the intermediate dimension of height, which is the largest extent of the current sheet in the plane perpendicular to the length. The longest dimension along the background magnetic field is length[30].

In this thesis, we aim at characterizing the current sheets formed in an x-y plane (the hybrid simulation plane) perpendicular to the background magnetic field. Therefore, here we describe the Zh-algorithm only for the determination of current sheet thickness and length. For calculating thickness of a current sheet the direction of the most rapid descent form the peak of the current sheet is determined by numerical calculating the Hessian matrix of parallel current density and its eigenvector at the peak. This is one of the fundamental methods of optimization which is widely used in the image processing. Hessian matrix is the second-order square matrix of partial derivatives of a scalar function. The Hessian matrix of parallel current density J_z at the point (x,y) is defined as follows:

$$\begin{pmatrix} \frac{\partial^2 J_z(x,y)}{\partial x^2}, \frac{\partial^2 J_z(x,y)}{\partial x \partial y} \\ \frac{\partial^2 J_z(x,y)}{\partial y \partial x}, \frac{\partial^2 J_z(x,y)}{\partial y^2} \end{pmatrix}$$

The direction of the eigevector associated with the largest magnitude eigen value of the Hessian gives the direction of the most rapid descent. Then distance in this direction from the current sheet peak to the point where current density drops to the value of $J_{min,i}$ is calculated. The same procedure is repeated in the opposite direction and the two distances are added to obtain the thickness of the current sheet. For obtaining the length, we calculate the longest distance between any pair of two points of a current sheet by iterating over all points in the xy cross section of the current sheet. This method is accurate unless the xy cross section is too much curved. It is also possible to use the method implemented for calculating the thickness of each current sheet, i.e., by using the second eigen vector of the Hessian matrix, to calculate length but it is less accurate because the current sheet boundary can be quickly reached due to the current sheet curvature.

3.4 Generating test data of current sheet in turbulence

We verify numerical implementation of the algorithm against test data of current sheets in turbulence generated by a mathematical function. The details of the turbulent current sheets in the test data are known and thus can be used to verify the results obtained by algorithm. The test data generator creates chosen number of current sheets with random location , orientation, size and peak current densities embedded in the background noise in a 2-D box . A 2-D current sheet can be generated with its center(the location of peak current density) at the intersection point (x_c, y_c) of two mutually

perpendicular lines $L_1$and L_2, and its sizes (L_{cs1}, L_{cs2}) along two lines using formula:

$$J_z(x,y) = J_{z_0}\text{sech}^2\left(\frac{x_1}{L_{cs1}}\right)\cdot\text{sech}^2\left(\frac{x_2}{L_{cs2}}\right) \tag{3.1}$$

The lines L_1 and L_2 are represented by equations:

$$L_1 : y - y_c = m_1(x - x_c) \tag{3.2}$$
$$L_2 : y - y_c = m_2(x - x_c) \tag{3.3}$$

The slope $m_1 = -1/m_2$ determines the orientation of current sheet.

Here x_1 and x_2 denotes the perpendicular distance of point(x, y) from line L_1 and L_2 respectively :

$$x_1 = (y - y_c - m_1(x - x_c))/\sqrt{1 + m_1^2} \tag{3.4}$$
$$x_2 = (y - y_c - m_2(x - x_c))/\sqrt{1 + m_2^2} \tag{3.5}$$

We choose N random values of each x_c,y_c, $m_1(m_2 = -1/m_1)$, J_{z0}, L_{cs1} and L_{cs2} to obtain N current sheet in a background turbulence using the expression:

$$J_z = \sum_{k=1}^{N}[J_{z0\,k}\text{sech}^2\left(\frac{x_{1\,k}}{L_{cs1,k}}\right)\text{sech}^2\left(\frac{x_{2\,k}}{L_{cs2,k}}\right)] + \text{Noise} \tag{3.6}$$

3.5 Code validation

For verifying the numerical implementation of Zh-algorithm [26] in the computer program, the program is applied on the test data of current sheet in turbulence. The test data consist of current sheets with random sizes, locations and orientations. The test data is generated using mathematical function for given current sheet parameters as described in the section 3.4.

There are several parameters which are needed for generating test data of current sheets in turbulence . One of the parameter is the background noise which can randomly change the randomly chosen but known locations(x_c, y_c) of the current density

peaks making them unknown and thus not allowing a verification of the identified peak locations. Therefore we will slowly increase the background noise from 1% to 10% of the peak current density. We generate N=10 current sheets in a box of size $128d_i \times 128d_i$ with a grid spacing of $0.5d_i$. The thicknesses L_{cs1} and L_{cs2} of current sheets (see Eq. 3.6) are chosen randomly from normal distributions with mean thicknesses $10d_i$ and $5d_i$ and standard deviations of $2.5d_i$. Peak current density J_{z0} of each current sheet is randomly chosen from a uniform distribution in the range from -1 to 1. The x and y position of each current sheet within the computational box is chosen from uniform distributions.

We carry out two sets of tests to check the accuracy of algorithm in detection of local maxima and current sheets. In the first set we choose a threshold value of the current density, $J_{thr} = J_{rms}$(Here J_{rms} denotes the root mean square of J_z), and $n = 3$. It means that the algorithm checks the magnitude of current density at a candidate point to be a local maxima in a region extended by three points on each side of the candidate point, i.e., a region of $(2n+1)^2 = 49$ data points. We choose the background noise level to be $J_{zmax}/100$ where J_{zmax} is the maximum peak current density. We focus on the positions of local maxima because finding the correct positions of local maxima is one of the first step to identify current sheet. Also analysis of difference between generated local maxima and identified local maxima gives appropriate feedback about the accuracy of algorithm. Figure 3.5 shows locations of chosen and identified maxima over plotted on color plot of the current density.

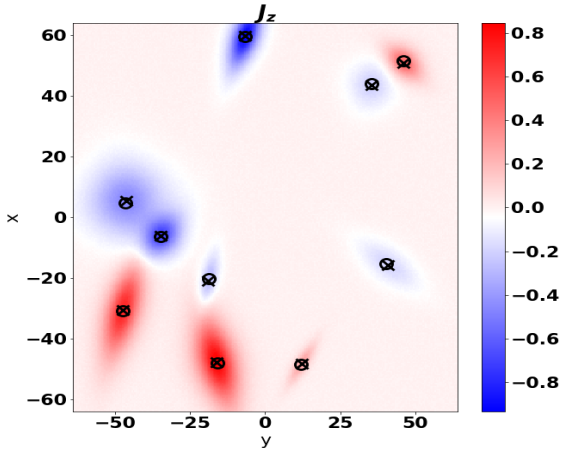

Figure 3.5: Test data of current density (color) generated for ten current sheets and background noise level $J_{zmax}/100$. Locations of current density peaks chosen to generate the test data are marked with 'x' while identied locations of the peaks are marked with 'o'. Here we choose n = 3 and $J_{thr} = J_{rms}$.The number of detected maxima are 10 from 10 generated current sheets.

As it can be seen from Fig 3.5 that the algorithm operates properly for noise level $J_{zmax}/100$ and number of detected and generated maxima is same (10 detected maxima out of 10 generated). However there are little differences between chosen and identified the positions of local maxima. In the next step we increase the background noise level to ($J_{zmax}/20$) and ($J_{zmax}/10$). Hence we can check how much back ground

noise affects the accuracy of the algorithm.

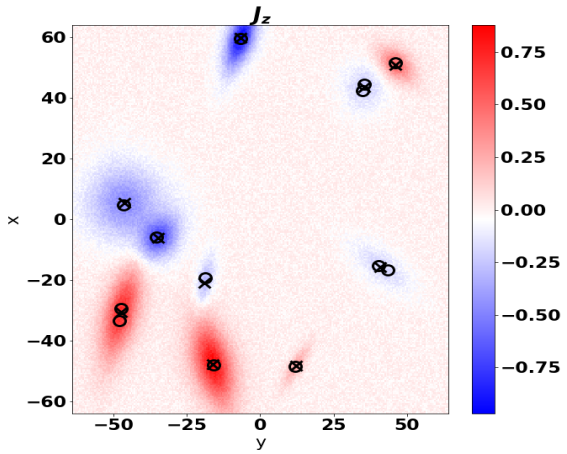

Figure 3.6: Test data of current density (color) generated for ten current sheets, and background noise level $J_{zmax}/20$. Locations of current density peaks chosen to generate the test data are marked with 'x' while identied locations of the peaks are marked with 'o'. Here parameters are n = 3 and J_{thr} = Jrms. The number of detected maxima are 13 from 10 generated current sheets.

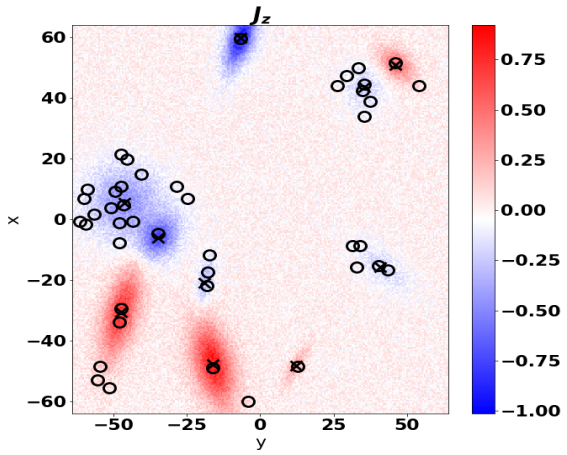

Figure 3.7: Test data of current density (color) generated for ten current sheets and background noise level $J_{zmax}/10$. Locations of current density peaks chosen to generate the test data are marked with 'x' while identied locations of the peaks are marked with 'o'. Here parameters are n = 3 and J_{thr} = Jrms . The number of detected maxima are 44 from 10 generated current sheets.

From Figure 3.6 and Figure 3.7 it can be seen that the generated data is not as smooth as in figure Figure 3.5 due to the enhancement of background noise. Also the number of the detected maxima exceeds the number generated maxima. For the noise level of level = $J_{zmax}/20$, the number of detected maxima is 13 while it is 44 for the noise level = $J_{zmax}/10$. Higher level of noise introduces additional peaks in the current density data. These peaks are, however, of no interest for current sheet detection and can be avoided by increasing the threshold current density J_{thr}.

In the second set of tests we increase the value of J_{thr} to $J_{thr} = 2J_{rms}$ with the same sequence of background noise. The results are shown in Figure 3.8-3-9.

From this set of tests we can see by increasing the value of J_{thr} in the first case with background noise (level = $J_{zmax}/100$), the number of detected maxima decreases to 8 unlike the same case for $J_{thr} = J_{rms}$ which was 10 out of 10 generated maxima. This is

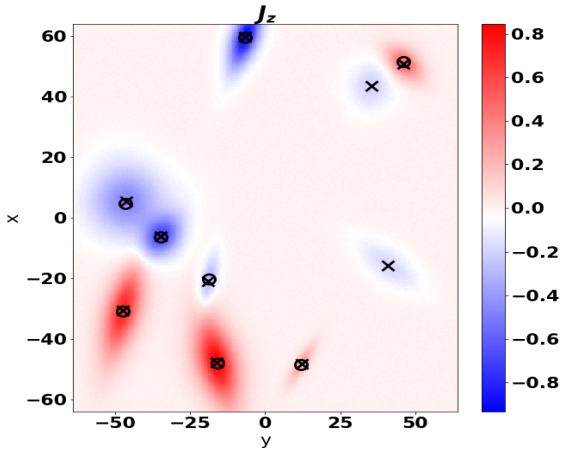

Figure 3.8: Test data of current density (color) generated for ten current sheets. Locations of current density peaks chosen to generate the test data are marked with 'x' while identified locations of the peaks are marked with 'o'. Here parameters are (noise = $J_{zmax}/100$) and $J_{thr} = 2Jrms$. The number of detected maxima is 8 from 10 generated current sheets.

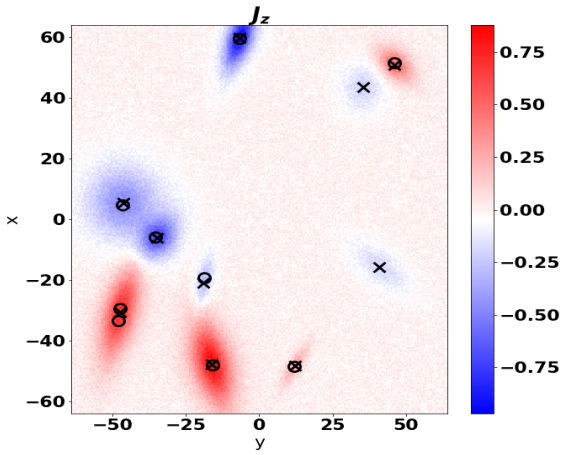

Figure 3.9: Test data of current density (color) generated for ten current sheets. Locations of current density peaks chosen to generate the test data are marked with 'x' while identified locations of the peaks are marked with 'o'. Here parameters are (noise = $J_{zmax}/20$) and $J_{thr} = 2Jrms$.The number of detected maxima is 9 from 10 generated current sheets.

because two of the ten maxima are below the threshold value of current density. Increasing the noise level to $J_{zmax}/20$, the number of detected local maxima increases to nine but still below the generated number of local maxima. Further increasing the noise level to $J_{zmax}/10$,the number of local maxima exceeds the generated number of maxima because now many of the local maxima due to the noise are above the threshold value.

These tests tell us that an appropriate value of J_{thr} for correct detection of current sheets depends on the background noise level. In an attempt to find a relationship between J_{thr} and the noise level, we vary for a test we varied the value of background noise level from 0.01 to 0.1 in step of 0.01 and the value of J_{thr}/J_{rms} . J_{thr}/J_{rms} from 0.5 to 10 in step of 0.5. The test data generator produces 10 current sheets. Figure 3.10 shows number of detected current sheets vs. J_{thr}/J_{rms} for various values of the background noise level. As expected, detection of correct number of sheets (ten sheets) requires higher value of J_{thr} for higher noise level. The value of J_{thr}, however, does not increase

in proportion of the noise level. The value of J_{thr} for the detection of correct number of current sheets changes by less than four times for an order of magnitude increase in the noise level from 1% to 10%. Therefore we can expect that $4J_{thr}/J_{rms} < 4$ would be sufficient for correct detection of current sheets in the hybrid simulation data. The value of J_{thr} and other parameters of the algorithm, however, should be chosen by varying them and examining their effect on the current sheet detection in a given data set.

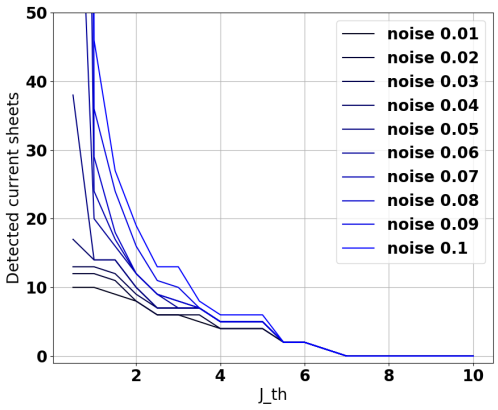

Figure 3.10: Number of detected current sheet vs J_{thr}/J_{rms} for 10 different values of back ground noise level.

Chapter 4

Characterization of current sheets in collisionless plasma turbulence

In this chapter we present the results obtained by applying the computer program developed for current sheet identification and characterization to the current sheet data produced by the hybrid simulation of collisionless plasma turbulence. The computer program implements Zh-algorithm described in chapter 3. Data from hybrid simulations with three different number of grid points, 512×512,1024×1024 and 2048×2048 are used. We first choose appropriate values of the three algorithm parameters for current sheet characterization in 512×512 simulations by examining the effects of the parameter variation on current sheet detection. The three algorithm parameters are threshold current density (J_{thr}), size of the local region around local maxima (n) and minmum current density for each current sheet (J_{min}). We also choose an appropriate value of the threshold on $u_{ez}/u_{iz,rms}$, the ratio of parallel electron bulk velocity and root-mean-square value of the parallel ion bulk velocity. This ratio will be used in addition to J_{thr} for cross verication of the characterization results. Next we statistically characterize current sheets in terms of their peak current densities, thicknesses, lengths and aspect ratios. Simulation data at three times around $\omega_{ci}t = 50$ will be used to establish the independence of the results on time. Robustness of the results against small variations of algorithm parameters around their chosen values is also checked. Finally, we examine the effect of the grid spacing in simulations on the characterization results.

4.1 Choosing algorithm parameters

4.1.1 Choosing J_{thr}, n and $u_{ez}/u_{iz,rms}$

Two of the algorithm parameters, the size of local region surrounding local maxima n and threshold current density J_{thr} (or $u_{ez}/u_{iz,rms}$) are required for finding the loca-

tions of local maxima in current density. Therefore we vary these two parameters to visually inspect if the locations of local maxima plotted over current density are more or less correct. Figure 4.1 shows the locations of local maxima found by the algorithm for $J_{thr} = J_{rms}$ and $2J_{rms}$ and n=5, 15 and 25.

As it can be seen from figure 4.1 that for $J_{thr} = J_{rms}$ and $n = 5$, algorithm found unreasonable number of local maxima. The reason is that for small values of threshold, the algorithm does not filter out fluctuations very well and many local maxima associated with these fluctuations are still present in the filtered data. Although peak current densities associated with the fluctuations are typically smaller than those associated with current sheets, they are not discarded by the algorithm as small values of n may not allow their comparison with the current sheet associated peaks. For larger value of threshold current density $J_{thr} = 2J_{rms}$ unwanted fluctuation peaks are filtered better and the impact is visually tangible for $n = 5$ in figure 4.1 . Also by keeping $J_{thr} = J_{rms}$ and increasing the value of n, the number of unwanted fluctuation peaks are reduced as many of them are now discarded in comparison to current sheet peaks. Figure 1.16 shows that not all but a reasonable number of peaks, sufficient for statistical analysis, are detected and results are almost the same for $J_{thr} = J_{rms}$ and $2J_{rms}$ when $n = 25$. We choose $J_{thr} = J_{rms}$ and $n = 25$ as appropriate values for current sheet characterization. Choosing a smaller value of J_{thr} reduces the risk of filtering out some of the low amplitude current sheet peaks and thus allowing a possibility of their detection.

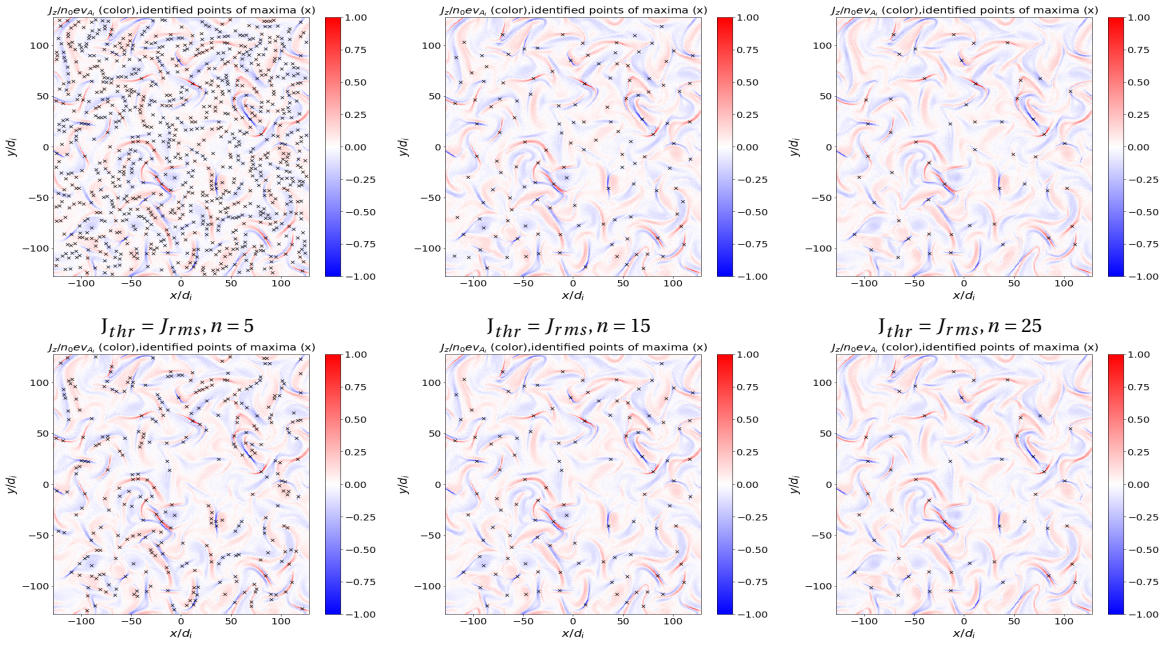

Figure 4.1: Parallel current density J_z (color) in the simulation plane at $\omega_{ci}\,t = 50$. Locations of local maxima (x) found by the algorithm are over plotted for $J_{thr} = J_{rms}$ (top row) and $2J_{rms}$ (bottom row). In a row, value of n increases, n=5, 15, 25 (left to right). The simulation box size has 512 × 512 grid points and 500 particles per cell. The time step is $\Delta t = 0.01\omega_{ci}^{-1}$.

Another method for filtering out background fluctuations is to use a threshold on

the ratio of parallel electron velocity u_{ez} over root mean square value of parallel ion velocity $u_{iz,rms}$ instead of threshold on current density. As it is discussed in chapter 2, u_{ez} is mach larger than u_{iz} in current sheets. Therefore large values of the ratio $u_{ez}/u_{iz,rms} \sim 5$ can be used as threshold. Fig 4.2 shows location of local maxima detected by the algorithm for $u_{ez}/u_{iz,rms} = 2.5$ and 7.25 and n=5, 15 and 25.

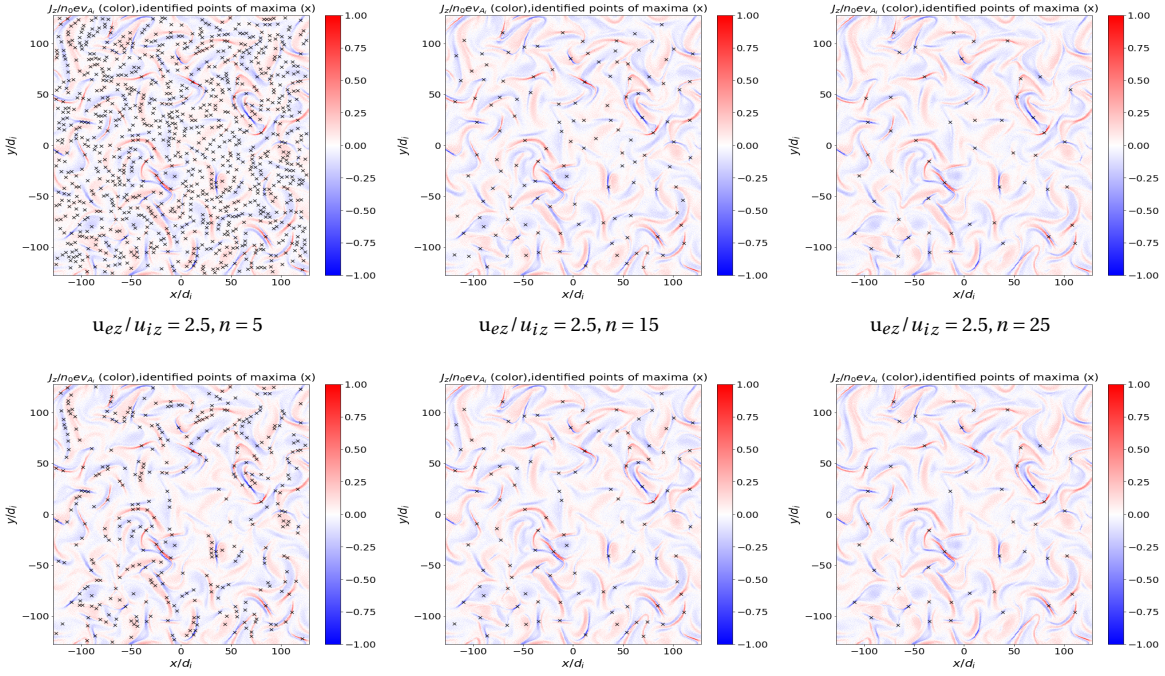

$u_{ez}/u_{iz} = 2.5, n = 5$ $u_{ez}/u_{iz} = 2.5, n = 15$ $u_{ez}/u_{iz} = 2.5, n = 25$

$u_{ez}/u_{iz} = 7.25, n = 5$ $u_{ez}/u_{iz} = 7.25, n = 15$ $u_{ez}/u_{iz} = 7.25, n = 25$

Figure 4.2: Parallel current density J_z (color) in the simulation plane at $\omega_{ci}t = 50$. Locations of local maxima (x) found by the algorithm are over plotted for $u_{ez}/u_{iz,rms} = 2.5$ (top row) and 7.25 (bottom row). In a row, value of n increases, n=5, 15, 25 (left to right). The simulation box size has 512×512 grid points and 500 particles per cell. The time step is $\Delta t = 0.01\omega_{ci}^{-1}$.

By comparison between two methods for choosing threshold value, we can see that in both methods, current sheet's peak points can be reasonably well detected for the sufficient size n of the region surrounding the peaks, n. Therefore we choose $n = 25$ in both methods and $J_{thr} = J_{rms}$ in the first method and $u_{ez}/u_{iz,rms} = 7.25$ in the second method.

4.1.2 Choosing minimum value of current density J_{min}

After the detection of peak location of current density for each current sheet, algorithm finds points which are collectively connected to the peak and have magnitude J_z above the J_{min} value (minimum value of current density). These points are defined as the current sheet points. Therefore value of J_{min} defines the boundary of current sheets. Here we choose value of $n = 25$ for the size of local region for both cases of the thresholds, $J_{thr} = J_{rms}$ and $u_{ez}/u_{iz,rms} = 7.25$, and $J_{min,i} = (0.4, 0.5, 0.6)J_{max,i}$ for each case ('i' is the current sheet index). Figure 4.3 shows the effect of changing $J_{min,i}$ on the identification of points belonging to each current sheet. The similarity in identified current

sheets for two cases of threshold value is apparent in figure 4.3. Also it can be seen that by increasing the $J_{min,i}$ value, the number of points belonging to each current sheet are decreased so as to reduce current sheet lengths. Figure 4.3 shows that appropriate values of $J_{min,i}/J_{max,i}$ for current sheets characterization are 0.4 and 0.5 and the results for these values should be compared. We, however, choose $J_{min,i}/J_{max,i} = 0.5$ in this thesis and defer the current sheet characterization for $J_{min,i}/J_{max,i} = 0.4$ to future work.

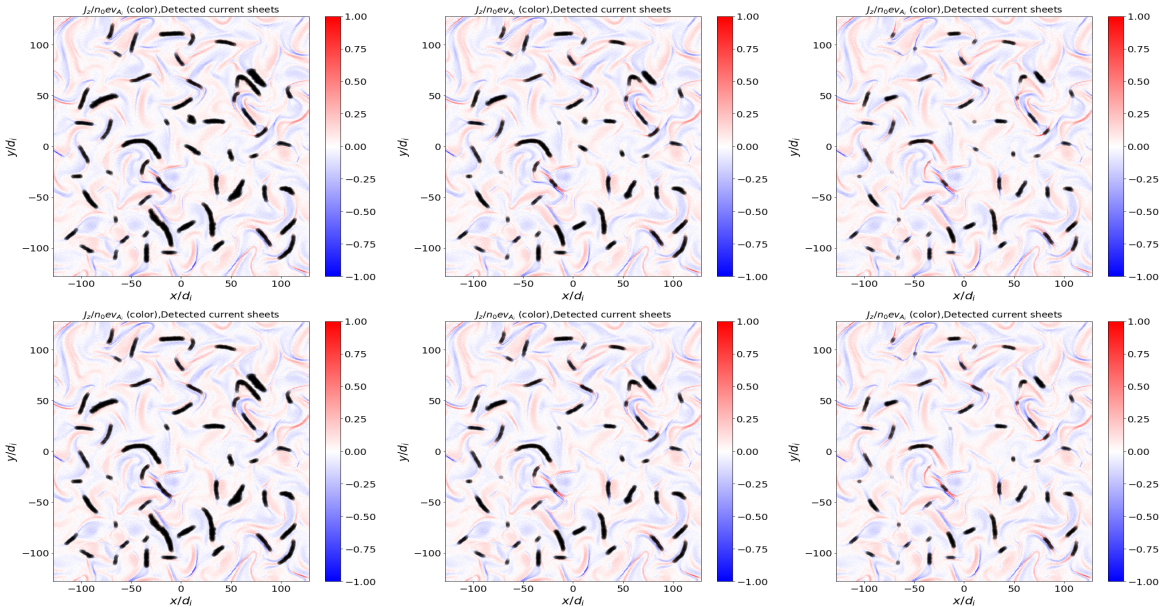

Figure 4.3: Detected current sheets by changing the J_{min} value. The top row of figures is for $J_{thr} = J_{rms}$ and $J_{min,i}/J_{max,i} = (0.4, 0.5, 0.6)$ (left to right). Bottom row for $u_{ez}/u_{iz,rms} = 7.25$ and $J_{min,i}/J_{max,i} = (0.4, 0.5, 0.6)$ (left to right).

4.2 Characterization of current sheets

We chose in section 4.1 appropriate values of threshold current density $J_{thr} = J_{rms}$, with size of the local region around current sheet peaks $n = 25$, $u_{ez}/u_{izrms} = 7.25$ and minimum current density $J_{min,i} = J_{max,i}/2$. We will use these values for the characterization of current sheets in terms of peak current density, thickness, length and aspect ratio. We check robustness of results against n and time by varying value of n around $n = 25$ and time around $\omega_{ci}\,t = 50$. By plotting distributions of thickness, length, aspect ratio (length/thickness) and peak current density of current sheet, we can understand about the type of instabilities and mechanism of energy dissipation from statistical point of view.

4.2.1 Peak current density

In figures 4.4, 4.5 and 4.6 we show the distributions of peak current density of current sheets at $\omega_{ci}t = (46, 50, 54)$ respectively, for $J_{th} = J_{rms}$ and compared it with $u_{ez}/u_{iz,rms} = 7.25$ as threshold value for $n = 20, 25, 30$.

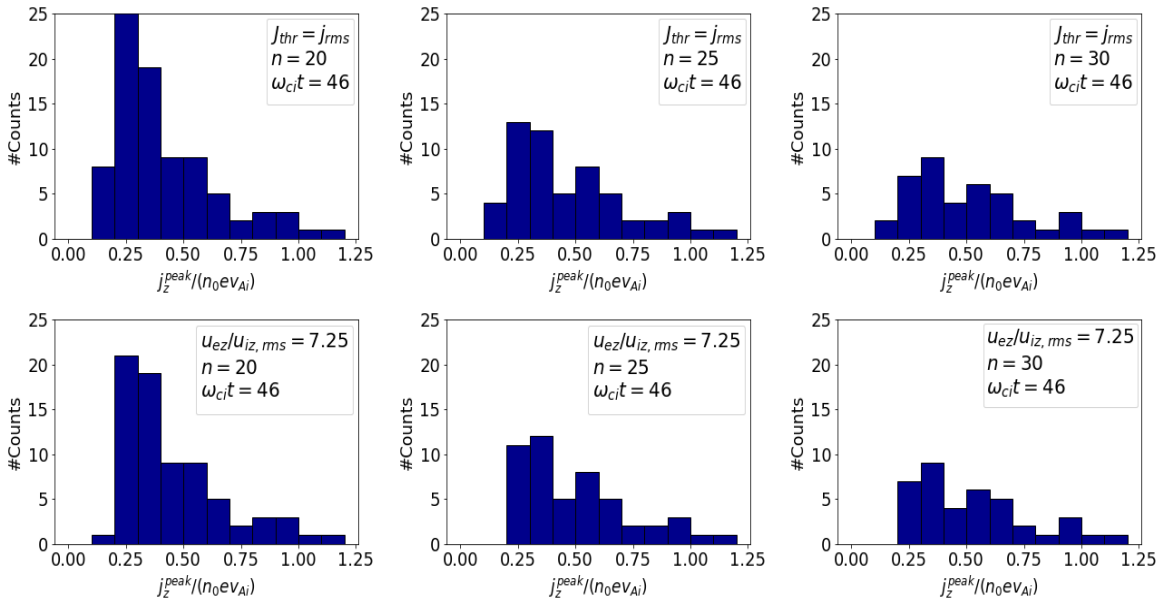

Figure 4.4: Distribution of peak current density at $\omega_{ci}t = 46$ For $J_{thr} = j_{rms}$ (top row) and $u_{ez}/u_{iz,rms} = 7.5$ (bottom row) with n=20, 25, 30 from left to tight.

For a given time and threshold, differences in distributions of peak current density can be noticed with the change in the value of n. Number of current sheets with small values of peak current density, approximately in the range 0.2-0.4, decreases with increasing value of n. This is because for large values of n the algorithm checks a data point to be a local maximum on a larger local region which may now include higher peaks of current density. Therefore, lower peaks of current density might be discarded in comparison to the higher peaks reducing their number. This, however, does not increase the number of current sheets with higher peaks. Under the variation of threshold and time, distributions of peak current density change but are more or less similar and allows to draw following conclusion. Majority of current sheets formed in the simulations with 512x512 grid points have peak current density in the range 0.2-0.4 $n_0 e v_{Ai}$ with maximum peak current density reaching up to 1.1 $n_0 e v_{Ai}$.

Parallel current density can be expressed as $J_z = \rho(u_{iz} - u_{ez})$ where ρ is the charge density. Therefore peak of parallel electron bulk velocity can be calculated from simulation data as $u_{ez,peak} = u_{iz,peak} - J_{z,peak}/\rho_{peak}$. In figure 4.7 the distribution of peak electron velocity in current sheets is shown at $\omega_{ci}t = 50$ for $J_{thr} = J_{rms}$ and $n = 20, 25, 30$. In figure 4.7, it can be seen that, similar to peak current density, most peaks of parallel electron bulk velocities are in the range 0.2 to $0.4 v_{Ai}$ with the maximum reaching 1.1 v_{Ai} and increasing the value of n reduces the number of current sheets in this range.

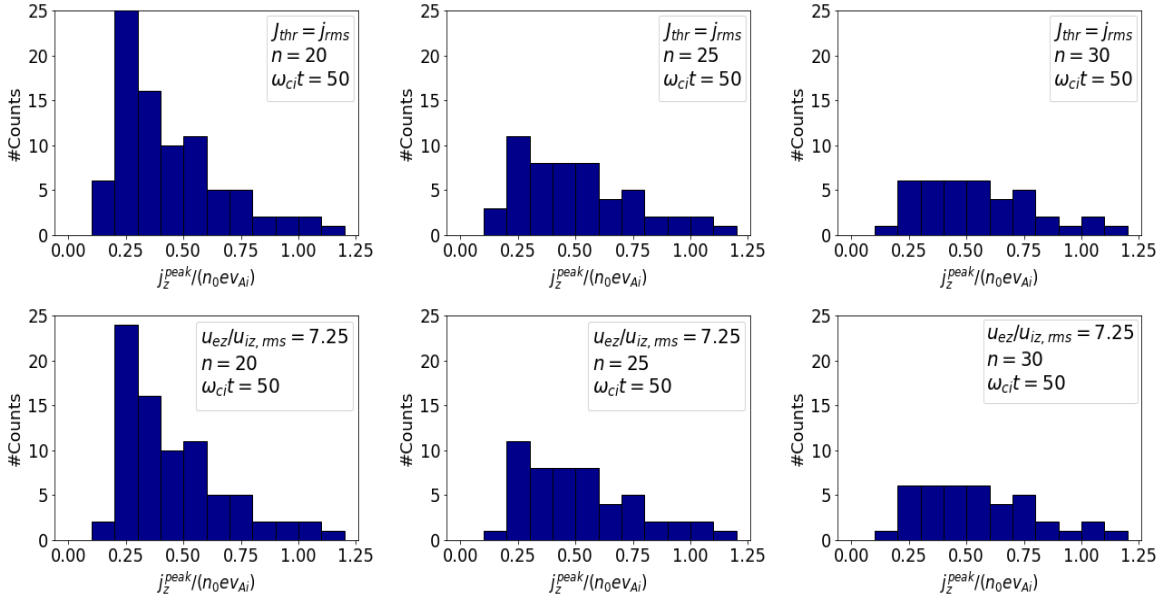

Figure 4.5: Distribution of peak current density at $\omega_{ci}t = 50$ For $J_{thr} = j_{rms}$ (top row) and $u_{ez}/u_{iz,rms} = 7.5$ (bottom row) with n=20, 25, 30 from left to tight.

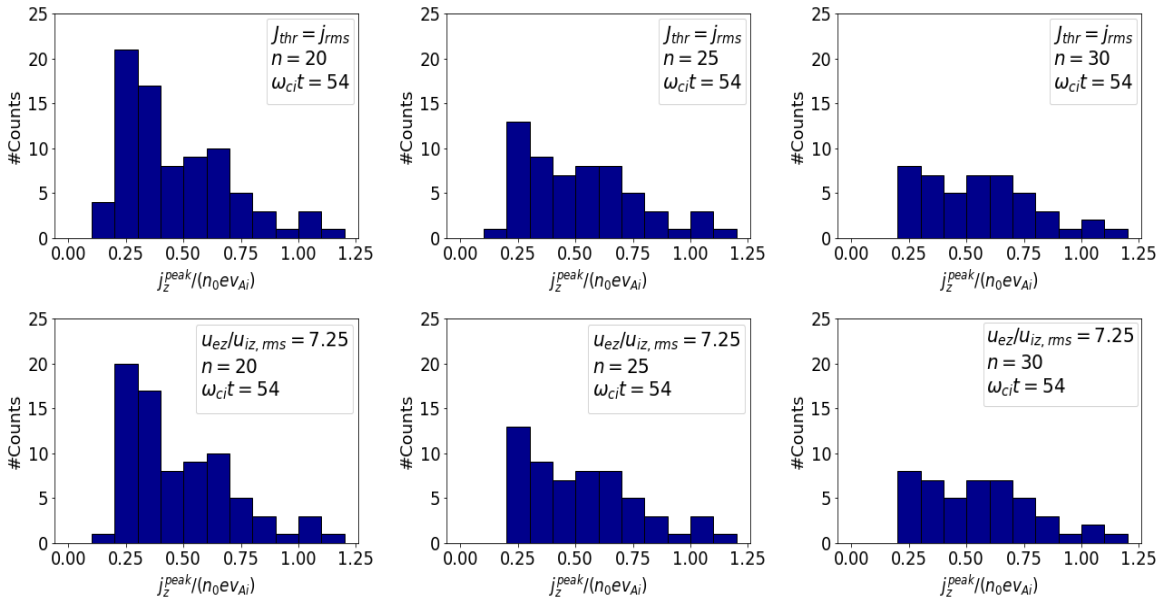

Figure 4.6: Distribution of peak current density at $\omega_{ci}t = 54$ For $J_{thr} = j_{rms}$ (top row) and $u_{ez}/u_{iz,rms} = 7.5$ (bottom row) with n=20, 25, 30 from left to tight.

The similarity in the distribution of peaks of current density and electron bulk velocity arises from the fact that ion bulk velocity is much smaller than electron bulk velocity and density normalized to background density is close to unity in current sheets (see chapter 2). Therefore current in the sheets is almost entirely due to the electron bulk velocity. The domination of electron velocity in the current sheets can give rise to the growth of streaming plasma instabilities driven by relative drift of plasma species (ion and electron).

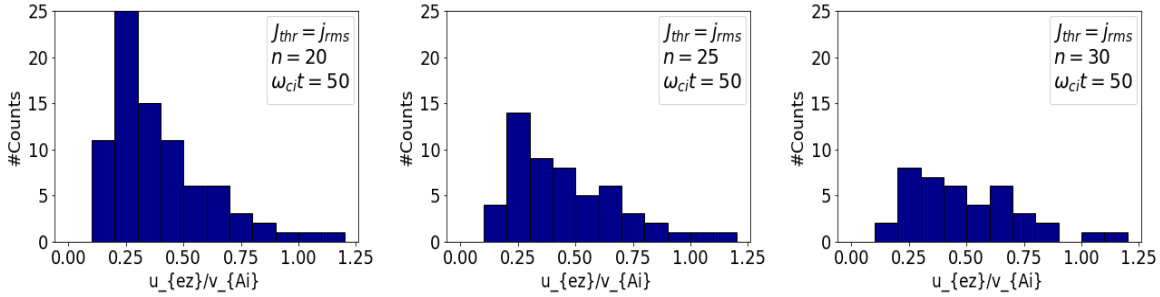

Figure 4.7: Distribution of the peaks of parallel electron velocity in curretn sheets for $n = 20, 25, 30$ (left to right) and threshold current density $J_{thr} = J_{rms}$. The time frame is chosen to be $\omega_{ci}t = 50$ at which the current sheets are well formed.

4.2.2 Thickness

Figures 4.8, 4.9 and 4.10 show distribution of current sheet thicknesses at $\omega_{ci}t = 46$, 50 and 54, respectively, for n=20, 25, 30 and different thresholds $J_{thr} = J_{rms}$ and $u_{ez}/u_{iz,rms} = 7.25$.

It can be seen from figures 4.8-4.10 that majority of current sheets have thicknesses close to 0.5 ion inertial length which is grid spacing for the simulation data. By increasing the value of n in the both cases of threshold, the number of current sheet with grid scale thicknesses decreases. It is due to the decline in the number of sheets for large values of n as low peak current sheets are discarded in comparison to high peak current sheets. However, if we compare distribution of thicknesses at different time , $\omega_{ci}t = 46, 50$ and 54 in figures 4.8, 4.9 and 4.10, the number of current sheets with grid scale thicknesses increase. This means that more and more current sheets getting thinner with time down to the grid spacing. In order to find the thicknesses down to which thinning processes continue, we will analyze simulations with higher grid resolutions in section 4.3.

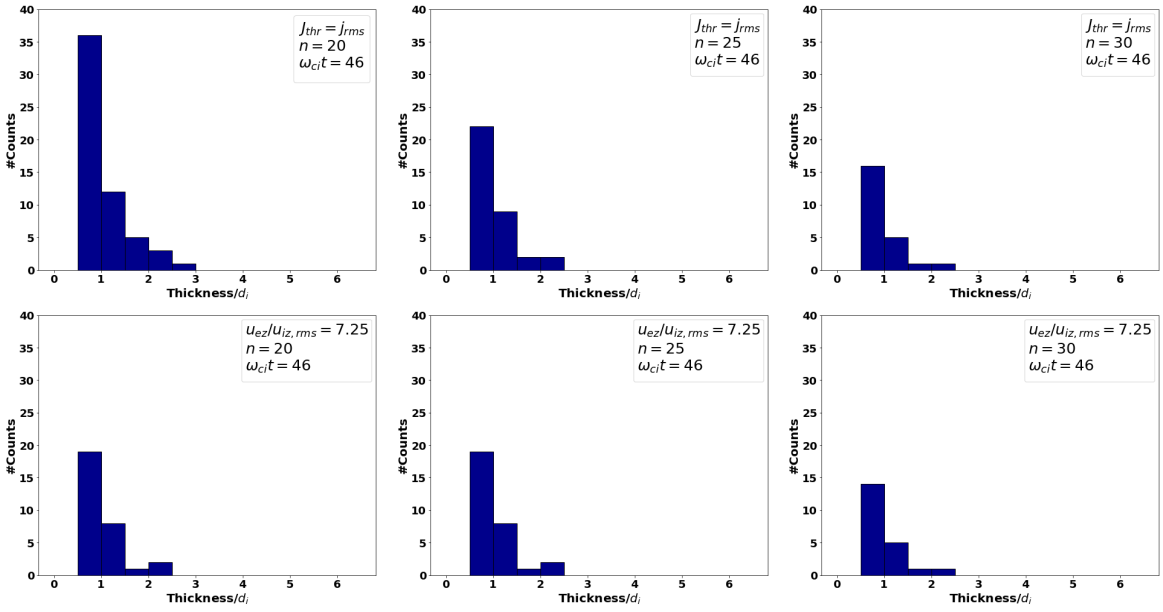

Figure 4.8: Distribution of half thickness of current sheets at $\omega_{ci}t = 46$ for $J_{thr} = j_{rms}$(top row) and $u_{ez}/u_{iz,rms} = 7.25$ (bottom row) with n=20, 25 and 30 from left to right.

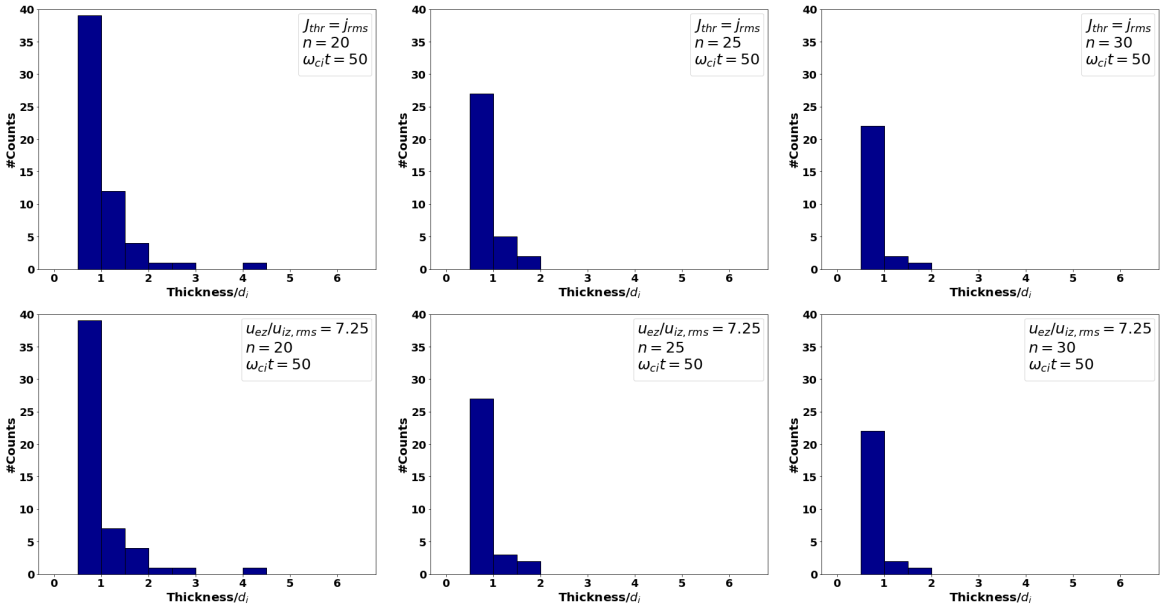

Figure 4.9: Distribution of half thickness of current sheets at $\omega_{ci}t = 50$ for $J_{thr} = j_{rms}$(top row) and $u_{ez}/u_{iz,rms} = 7.25$ (bottom row) with n=20, 25 and 30 from left to right.

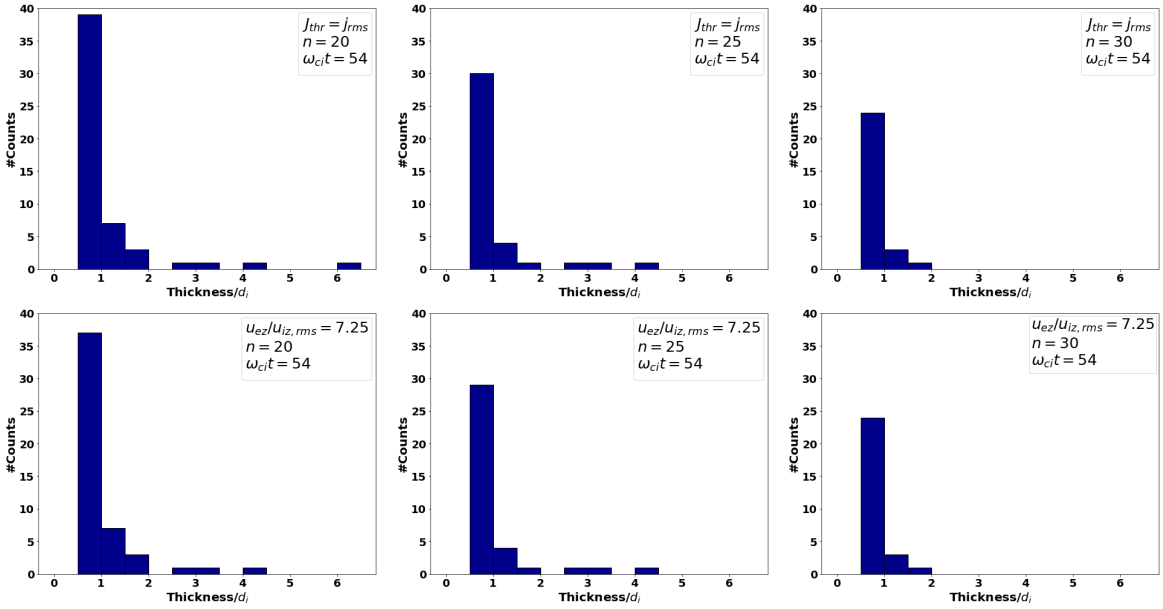

Figure 4.10: Distribution of half thickness of current sheets at $\omega_{ci}t = 54$ for $J_{thr} = j_{rms}$(top row) and $u_{ez}/u_{iz,rms} = 7.25$ (bottom row) with n=20, 25 and 30 from left to right.

4.2.3 Length

Another characterization of current sheets is in the terms of length. Figures 4.11 to 4.13 show that majority of current sheets have length in the range of $5d_i$ to $25d_i$, mostly around $15d_i$. By comparison of figures 4.11, 4.12 and 4.13, it is clear that with time, number of current sheets with lengths of $5d_i$ to $25d_i$ is not significantly changing. Although some current sheets have maximum length of $40d_i$ the majority of lengths are concentrated in the specific range $5d_i$ to $25d_i$.

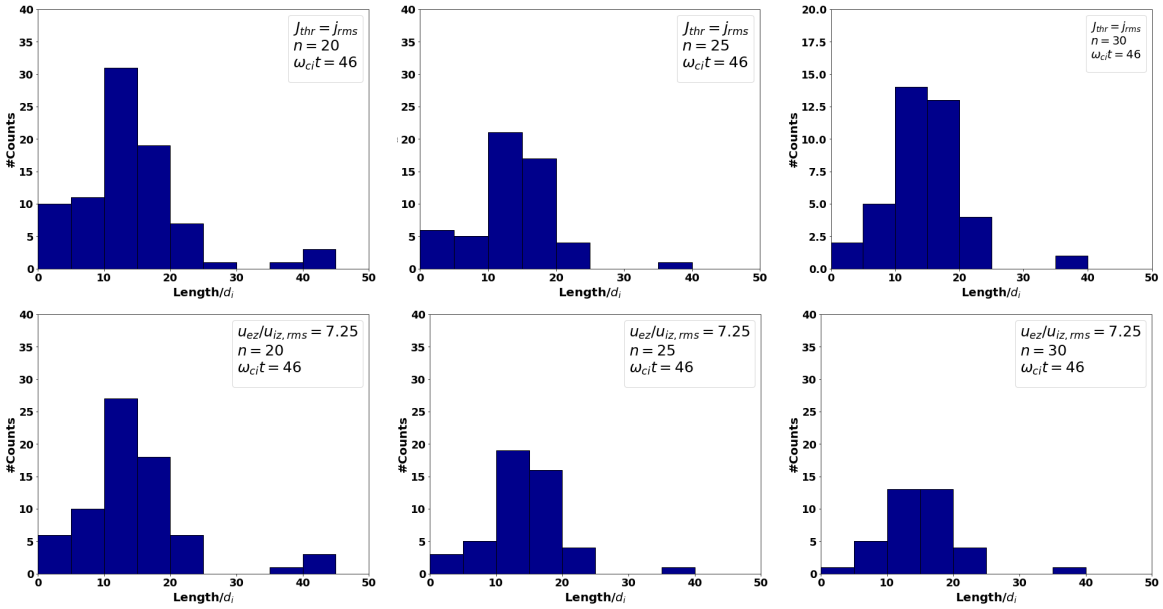

Figure 4.11: Distribution of current sheets length at $\omega_{ci}t = 46$ for $J_{thr} = j_{rms}$(top row) and $u_{ez}/u_{iz,rms} = 7.25$ (bottom row) with n=20, 25 and 30 from left to right.

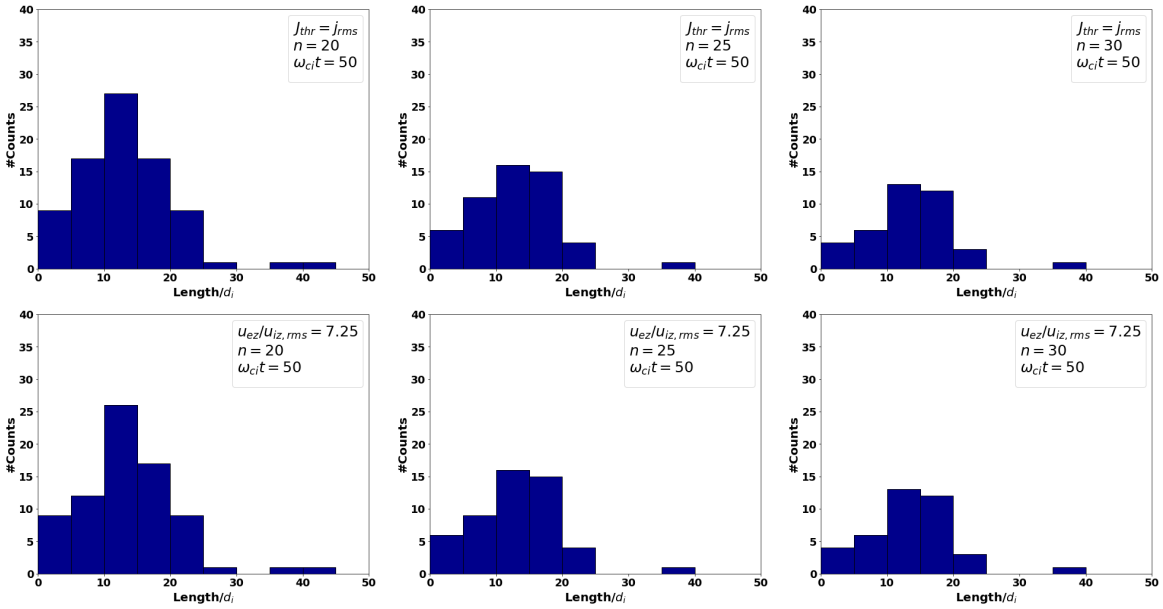

Figure 4.12: Distribution of current sheets length at $\omega_{ci}t = 50$ for $J_{thr} = j_{rms}$(top row) and $u_{ez}/u_{iz,rms} = 7.25$ (bottom row) with n=20, 25 and 30 from left to right.

Aspect ratio

For spatial gradient driven instabilities, the ratio of the length and half-thickness of current sheets is an important parameter. We characterize the ratio of length over thickness (aspect ratio) in figures 4.14-4.16. In figure 4.14, by increasing the value of n the number of current sheets decreases and similarity between two types of threshold current density is clear. By comparing the aspect ratio of current sheets at three different times frame in figure 4.14,4.15 and 4.16, we can see that the values of aspect

ratio for majority of current sheets are concentrated in the range of 10 to 40 and some of the aspect ratio's values are greater than this range.

At the end of characterization of current sheets for 512 × 512 simulation, it is concluded that regardless of the algorithm parameters such as threshold current density J_{thr}, size of the region to find local maxima n, and minimum current density J_{min}, the distributions shows similar results from the statistical point of view.

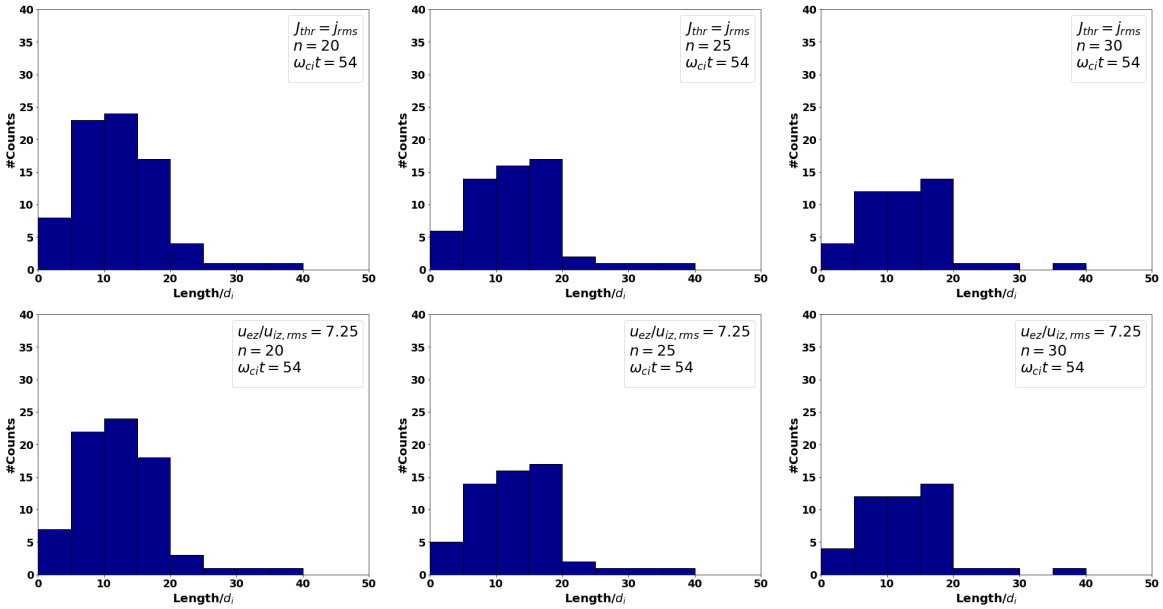

Figure 4.13: Distribution of current sheets length at $\omega_{ci}t = 54$ for $J_{thr} = j_{rms}$(top row) and $u_{ez}/u_{iz,rms} = 7.25$ (bottom row) with n=20, 25 and 30 from left to right.

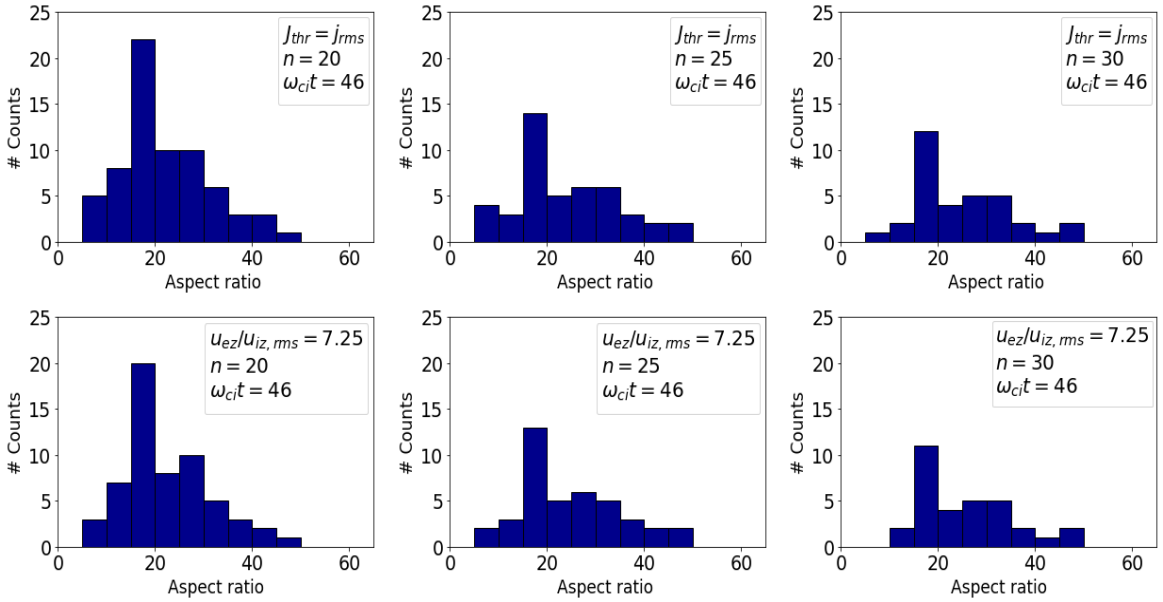

Figure 4.14: Distribution of aspect ratio of current sheets at $\omega_{ci}t = 46$ for $J_{thr} = j_{rms}$(top row) and $u_{ez}/u_{iz,rms} = 7.25$ (bottom row) with n=20, 25 and 30 from left to right.

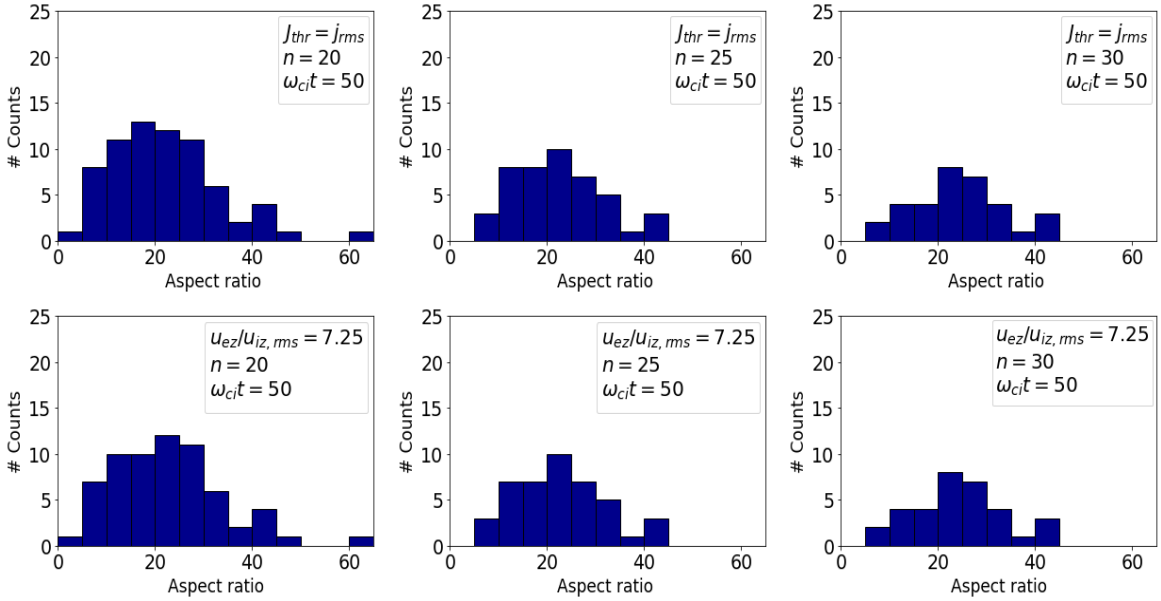

Figure 4.15: Distribution of aspect ratio of current sheets at $\omega_{ci}t = 50$ for $J_{thr} = j_{rms}$(top row) and $u_{ez}/u_{iz,rms} = 7.25$ (bottom row) with n=20, 25 and 30 from left to right.

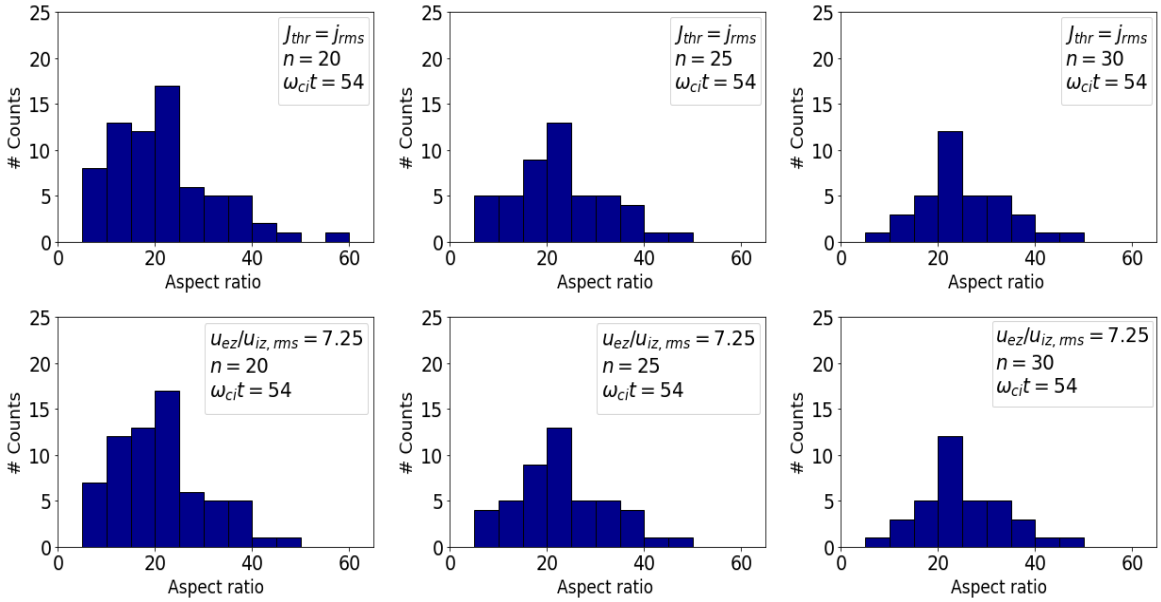

Figure 4.16: Distribution of aspect ratio of current sheets at $\omega_{ci}t = 54$ for $J_{thr} = j_{rms}$(top row) and $u_{ez}/u_{iz,rms} = 7.25$ (bottom row) with n=20, 25 and 30 from left to right.

4.3 High resolution data

2-D hybrid simulations of kinetic plasma turbulence and the characterization results show the formation of current sheets which thin down to grid scale. This indicates that majority of current sheets become thinner if we allow them by taking high grid resolution. For investigation about the reduction in thickness to grid scale we use high resolution hybrid simulations with 1024×1024 and 2048×2048 grid points.

Here we show the distributions of the peaks of J_z and half-thickness in figures 4.17 and 4.18 , respectively, at three times $\omega_{ci}t = (40, 50, 60)$. In figure 4.17, it is clear that

peaks of histograms shift to larger values of peak current density as the grid spacing decreases. It means that with the thinning of current sheets, as shown by figure 4.18, the peak current density increases.

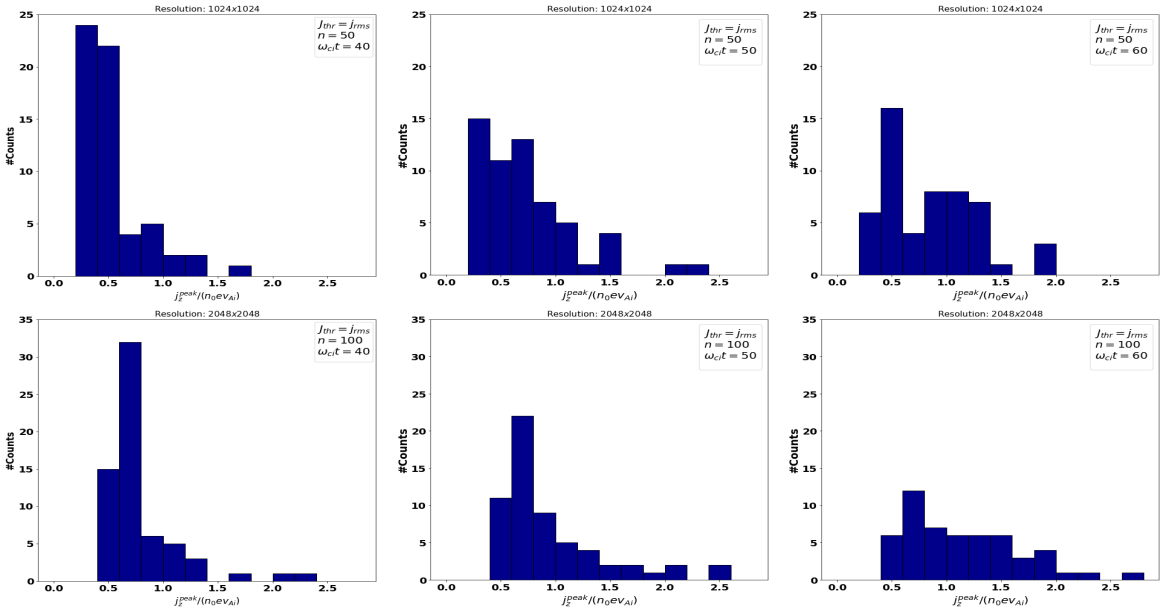

Figure 4.17: Distribution peak current density

We double and quadruple the value of n for 1024×1024 and 2048×2048 simulations, respectively, to keep the physical dimensions of the local region same. In figure 4.18 we compare the distribution of thickness for two high resolutions data,1024×1024 and 204×2048. As it can be seen that most current sheets have thicknesses close to the grid spacing for 1024×1024 and 2048×2048 data. It means current sheets want to thin down as much as possible within the framework of the hybrid plasma model.

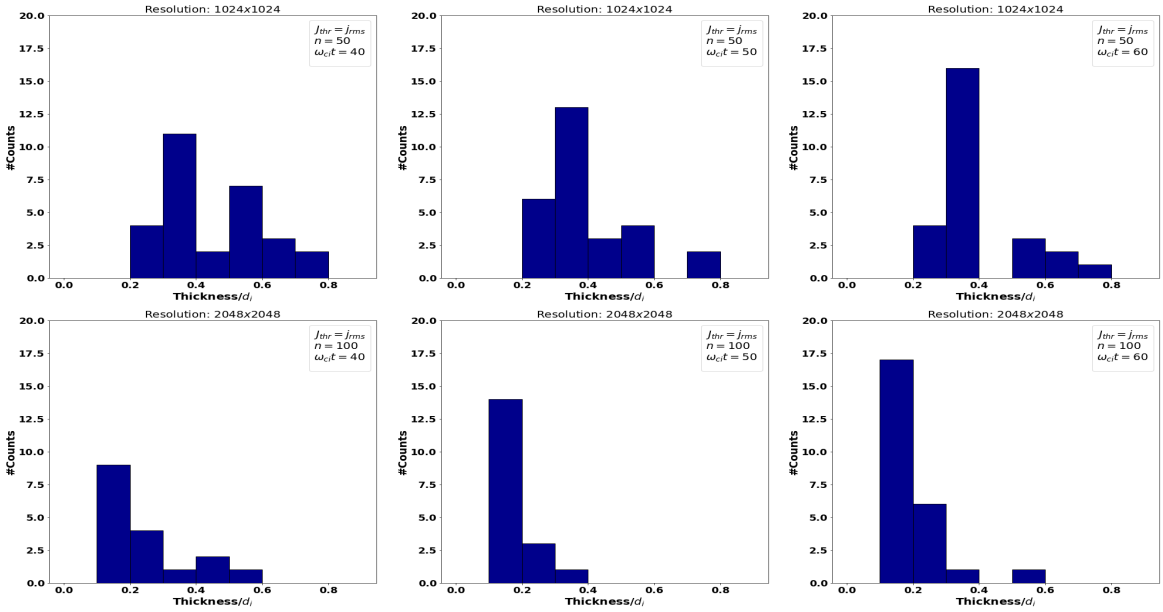

Figure 4.18: Distribution of half thickness for data 1024x1024 in top and 2048x2048 in below.

Chapter 5

Summary and discussion

This chapter presents an overall summary of this research work , its limitations, physical interpretations of the obtained results within the limitations and future directions.

5.1 Summary

The aim of this thesis is to develop a computer program to identify and characterize current sheets in plasma turbulence, verify the program against test problems and then apply it to the data obtained from PIC-hybrid simulations of collisionless plasma turbulence to characterize current sheets formed therein. Current sheets form self-consistently at kinetic scales in collisionless plasma turbulence and are the sites of the dissipation of the turbulence energy. Plasma processes responsible for the dissipation in current sheets formed in collisionless plasma turbulence are either directly or indirectly influenced by plasma instabilities in current sheets which depend on the available free energy sources, structure and physical parameters of current sheets. Therefore characterization of current sheets formed in collisionless plasma turbulence in terms of their free energy sources, structure and physical parameters is important to understand collisionless dissipation mechanism.

In this thesis, we developed from scratch a python code for identification and characterization of current sheets in collisionless plasmas turbulence based on the algorithm of Zhdankin et al.(2013)[26]. This algorithm has two parts. First part is the identification of current sheets and second is the characterization part. The algorithm identifies current sheets in turbulence by first removing the background current density fluctuations below a certain threshold value J_{thr} (typically few times the root-mean-square value of the current density) and then detecting current density peaks by searching for current density values which are local maxima in a surrounding local region containing $(2n+1)^2$ grid points. The points continuously connected to a peak current density and have values of current density above a minimum value J_{min} are collected as points

belonging to a current sheet associated with the current density peak. Second part of the algorithm is the characterization of current sheets in terms of their thicknesses and lengths. We have achieved this by using Hessian matrix of current density and its eigenvectors for calculation of thickness and finding the largest distance between any pair of current points for each current sheet as the length. The newly developed python code was benchmarked against test data which generates a given number of current sheets with controlled parameters and tunable back ground noise by the means of mathematical formula.

We applied the pyhton code to the current density data obtained from the hybrid simulation of collisionless plasma turbulence to characterize current sheets formed therein. The data was chosen at a time when current sheets have more or less formed but have not yet become distorted. We then selected appropriate values for the three algorithm parameters, viz., J_{th}, n and J_{min}, and also $u_{ez}/u_{iz,rms}$ (the ratio of parallel electron bulk velocity and root-mean-square value of the parallel ion bulk velocity used as threshold to cross-check the results obtained with J_{th}) by varying them and checking for a reasonably good identication of current sheets (Figures 4.1-4.3). Dependence of the results on the value of n and time around the selected time was studied.

The characterization results show that current sheets thin down to the grid scale ($< d_i$) and have tendency to be thinner as was shown by characterization of current sheets formed in high resolution hybrid simulations (Figures 4.8-4.10, 4.18). With the current sheet thinning, peak current density enhances (Figure 4.17). The distributions of the peaks of current density and parallel electron bulk velocity in current sheets are similar (Figures 4.4-4.7), consistent with the observations already made in the simulations that electrons are main current carrier in current sheets. Majority of current sheets have lengths of the order of 20 d_i (Figures 4.11-4.13) and thus a large aspect ratio (Figures 4.14-4.16) as their thicknesses are below ion inertial length.

5.2 Limitation

The results obtained in this thesis have some limitations for their applicability to physical systems, e.g., solar wind. These limitations are mainly due to the following reasons.

5.2.1 Two dimensionality

In this work, we characterized current sheets in terms of their peak current density, thickness, length and aspect ratio in two dimensional plasma turbulence in which variations along the direction of the large scale magnetic field, and thus also along the direction of the current in the sheets, were neglected. Physical systems are, however, three dimensional. Plasma waves and instabilities (e.g., lower hybrid drift instability,

kink instability and modified two stream instabilities - see[22] for discussion of these and related instabilities) with wave vector components along the electric current and large scale magnetic field may influence the properties of current sheets in physical systems. If these plasma instabilities grow in current sheets under formation in 3-D plasma turbulence, they can stop, for example, the further thinning of current sheets. As a result, current sheets in 3-D plasma turbulence might have thicknesses (also other properties of current sheets as a consequence of the 3-D effects) different from those found in 2-D simulations. Three dimensional simulations of collisionless plasma turbulence and characterization of current sheets formed therein are required to validate the results obtained from 2-D simulations.

5.2.2 Neglect of electron scale physics:

Another limitation of the results obtained in this thesis is the neglect of electron scale physics in the hybrid simulations of collisionless plasma turbulence data of which was used for the current sheet characterization. Neglect of electron scale physics is justified for scales much larger than the electron scales. The results of current sheet characterization, however, show that current sheets formed in 2-D plasma turbulence thin down to below ion scales and that the thinning of current sheets is limited by the grid spacing used in the simulations. In a physical system where thinning is not limited by grid spacing, current sheets may continue to thin down to electron scales. Hybrid simulations with electron scale grid resolution will not be useful to determine the final thicknesses of current sheets because the simulations do not contain physics at the electron scales. Simulations of collisionless plasma turbulence employing plasma models which include the electron scale physics (for example, hybrid plasma model with electron inertia) and characterization of current sheets formed therein are required to correctly determine the properties of the current sheets.

5.3 Physical interpretation

5.3.1 Current sheets thinning to electron scales

The results presented in this thesis can be physically interpreted within the limitations discussed in section 5.2. Although plasma instabilities with parallel wave vector components are not allowed to grow in the current sheets formed in the 2-D hybrid simulations of collisionless plasma turbulence, there is no such restriction on the growth of the 2-D ion-scale plasma instabilities with perpendicular wave vectors. Here the "perpendicular" and "parallel" directions are with respect to the large scale magnetic field. Our results of current sheet characterization show that current sheets continue to thin

down below ion inertial length as much as allowed by the grid resolution of the hybrid simulations and then get distorted by artificial numerical effects (Fig. 2.1 in chapter 2). It means current sheets prefer to thin down below ion inertial length rather than develop 2-D ion-scale plasma instabilities with perpendicular wave vectors. This is in contrast with other hybrid simulations of collisionless plasma turbulence in which current sheets formed in the turbulence do not thin down below ion inertial length but develop perpendicular tearing instability leading to magnetic reconnection when their thicknesses are close to the ion inertial length (much larger than grid scale) [31, 32]. This difference is due to the values of plasma resistivity used in the hybrid simulations. In other hybrid simulations [31, 32], value of the plasma resistivity is fine tuned to set the dissipation scale length close to an ion inertial length causing development of tearing instability when current sheets thin down to ion inertial length. On the other hand, in the hybrid simulations used in this thesis, plasma resistivity has been chosen to be zero (with a very small time step to stabilize the wave modes at the grid scales) not allowing the growth of the tearing instability. Instead, current sheets continue to thin down to below ion inertial length. The use of plasma resitivity in hybrid simulations is for the numerical purposes and thus is artificial. Owing to much smaller plasma resistivity in most physical system, current sheets therein are likely to thin down below ion inertial length (if not hindered by 3-D ion scale plasma instabilities) rather than developing 2-D tearing instabilities. Physical meaning of continuous thinning of current sheets below ion inertial length is that the current sheets will ultimately thin down to electron scale lengths where the thinning can be stopped by physical effects, for example, by finite electron inertia, rather than artificial resistivity.

5.3.2 Implications for plasma instabilities at electron scales

Plasma instabilities may grow in the electron scale current sheets expected to form by the continuous thinning below ion inertial length in collisionless turbulent plasmas, limiting the current sheet thicknesses and providing dissipation. Plasma instabilities are driven unstable by free energy sources provided by either the spatial gradients of macroscopic variables and/or non-Maxwellean features of plasma particles distribution function. The hybrid simulations used for current sheet characterization in this thesis show the development of electron shear flow and relative streaming of electron and ions as free energy sources in current sheets [33] which coupled with the characterization result of current sheet thinning down to electron scales implies the possibilities of electron inertia driven electron shear flow and parallel-wavevector electron-ion streaming instabilities in electron scale current sheets of collisionless plasmas turbulence. These instabilities can not be observed in the hybrid simulations used in this thesis due to their limitations arising from neglect of electron inertia and parallel vari-

ations. We discuss below possibility of these two instabilities in electron scale current sheets formed in collisionless plasma turbulence in physical systems.

(A) Electron shear flow instabilities Electron shear flow instabilities (ESFI) [34] have primarily been studied using an electron-magnetohydrodynamic model (EMHD) which is nothing but the stationary ions limit of the hybrid plasma model with the inclusion of electron inertia. The EMHD model is valid for space and time scales much smaller than the ion characteristic scales and thus suitable for the study of electron scale phenomena in fluid approximation. ESFI grows as a tearing instability for weak guide magnetic field (parallel to the direction of electron flow/current) and/or current sheet thickness less than or of the order of an electron inertial length [34]. It grows as a non-tearing instability for strong guide field and/or thicker current sheets [34].

Since current sheets in collisionless plasma turbulence thins down from thicknesses much larger than an electron inertial length, they are susceptible to non-tearing ESFI as long as thicknesses do not reduce to an electron inertial length. Non-tearing ESFI, however, may not grow if the thinning process is faster than the instabilities. In that case, current sheets are expected to thin down to electron inertial length or below and the tearing ESFI can grow leading to magnetic reconnection at electron scales.

For the tearing ESFI to grow in a current sheet of half-thickness L_{cs}, the unstable wave number k along the current sheet length must satisfy $kL_{cs} < 1$ [35]. In terms of the wavelength $\lambda = 2\pi/k$, the instability condition becomes $\lambda/L_{cs} > 2\pi$, implying that the current sheet must have enough length l_{cs} to accommodate long wavelengths. For $\lambda \sim l_{cs}$, we get a condition on the aspect ratio l_{cs}/L_{cs} of the current sheet.

$$\frac{l_{cs}}{L_{cs}} > 2\pi$$

Results of the current sheet characterization in chapter 4 show that majority of the current sheets have the aspect ratio ~ 20 even when their thicknesses are of the order of ion inertial length. Thinner current sheets, as expected in collisionless plasma turbulence, would have much larger asppect ratios and can therefore become unstable to the tearing ESFI if thickness reaches an electron inertial length. New simulations using plasma models which include the physics at electron scales, for example, particle-in-cell simulations or hybrid simulations with electron inertia, need to be carried out to decide the final fate of current sheets in collisionless plasma turbulence.

(B) Electron-ion streaming instabilities In an electron ion plasma with equal temperature for both the species, an electron-ion streaming instability can be excited if the relative streaming speed is larger than the electron thermal speed which can be obtained from electron plasma beta.

$$v_{th} = \sqrt{\frac{m_i}{m_e}\frac{\beta_e}{2}}v_{Ai},$$

where m_i and m_e are ion and electron masses respectively. The instability condition on the relative streaming speed $u_{ez} - u_{iz} \approx uez > v_{the}$ can then be written as,

$$\frac{u_{ez}}{v_{Ai}} > \sqrt{\frac{m_i}{m_e}\frac{\beta_e}{2}} \tag{5.1}$$

Characterization of current sheets in chapter 4 shows that the value of parallel current density and thus u_{ez} in current sheets increases with the thinning of current sheets. Since $u_{ez} \gg u_{iz}$, a scaling of u_{ez} with L_{cs} can be estimated from Ampere's law as,

$$\frac{u_{ez}}{v_{Ai}} \sim \sqrt{\frac{m_i}{m_e}}\frac{d_e}{L_{cs}}\frac{|B_\perp|}{B_0} \tag{5.2}$$

For $L_{cs} \sim d_e$ and $|B_\perp|/B_0 \sim 1$, Eq. (5.4) gives $u_{ez}/v_{Ai} \sim \sqrt{m_i/m_e}$ which can satisfy the instability condition (5.1) for $\beta_e < 1$. For $\beta_e = 0.5$, the value used in our hybrid simulations, electron-ion streaming instability might be important if current sheets thin down to the electron inertial scale.

5.4 Future directions

In this work, we developed a python code for the identification and characterization of current sheets in turbulence and applied it to characterize current sheets formed in hybrid simulations of collisionless plasma turbulence. We characterized the current sheets in terms of peak current density, thickness, length and aspect ratio and the results provide insights in the nature of current sheets in collisionless plasma turbulence. More research in the directions of code development and characterization of current sheets, however, needs to be done to fully understand the role of current sheets in collisionless plasma turbulence. We discuss below several possibilities for further research.

5.4.1 Code development

Handling data near boundaries — The Zhdankin's algorithm of current sheet identification checks if a current density at a candidate point is a local maxima in the surrounding region extended n points on both sides of the candidate point in the x- and y-directions. If a candidate point is less than n points away from any of the boundaries, the surrounding local region would extend beyond that boundary. In order to

avoid this, the points less than n points away from the boundaries are not considered as candidate points to be local maxima. This does not cause significant errors in the statistical characterization of current sheets as the value of n is much smaller than total number of grid points. It is, however, desirable to include in the analysis the points near the boundaries by taking in to account boundary conditions of the simulations.

Extension to other coherent structures — Current sheets are not the only coherent structure found in collisionless plasma turbulence. Several other types of coherent structures, e.g., plasmoids, flux ropes and vortices are also important and may contribute to collisionless dissipation. Extension of the code to identify and characterize these structures would help to understand the relative roles of coherent structures in plasma turbulence.

Extension to 3-D— The developed code identifies and characterizes current sheet in 2-D plane perpendicular to the mean magnetic field. Plasma turbulence and coherent structures in it are, however, three dimensional. Therefore, extension of the code to three dimensions is highly desirable.

5.4.2 Current sheet characterization

Identification of current sheets give access to the points belonging to current sheets and therefore other physical quantities at these points and their relations with current sheets can be characterized.

Temperature anisotropy— In simulations, temperature anisotropy (different temperatures parallel and perpendicular to the mean magnetic field) is found to be associated with current sheets. It is another free energy source that can give rise to kinetic plasma instabilities in current sheets and influence the growth of other instabilities, and is therefore important for characterization.

Vorticity— Development of vorticity near current sheet is often observed in kinetic simulations. It can give rise to Kelvin-Helmholtz like shear flow instabilities and can influence other instabilities in current sheets. It is also not clear how exactly current sheets and vorticity are related in plasma turbulence. A characterization of current sheets and vorticity will help answer these questions.

Relationship between heating and vorticity Heating of plasma in collisionless plasma turbulence is correlated with vorticity much more strongly than current sheets. Infact, sign of the vorticity has been observed in kinetic simulations to be related to the heating or cooling and nature (parallel or perpendicular) of the temperature anisotropy[36].

J.E— A part of the work done by electric fields on the particles is used in heating the plasma. The relative contribution of parallel and perpendicular field in the total work done in current sheets is an active topic of research [37]. Its characterization would help to understand the processes in current sheets responsible for the dissipation.

Current sheets heights—- In three-dimensional turbulence, current sheets will have finite height (size parallel to the mean magnetic field). Characterization of current sheets height would allows us to understand the possibilities of plasma instabilities with wave numbers parallel to the mean magnetic field.

Bibliography

[1] J. E. Borovsky and S. P. Gary, "Electron-ion coulomb scattering and the electron landau damping of alfvén waves in the solar wind", Journal of Geophysical Research: Space Physics **116**, A07101 (2011).

[2] M. J. Aschwanden, *Physics of the solar corona. an introduction with problems and solutions (2nd edition)* (Springer-Verlag Berlin Heidelberg, 2005).

[3] O. Alexandrova, J. Saur, C. Lacombe, A. Mangeney, J. Mitchell, S. J. Schwartz, and P. Robert, "Universality of solar-wind turbulent spectrum from mhd to electron scales", Phys. Rev. Lett. **103**, 165003 (2009).

[4] X. Wang, C. Tu, J. He, and L. Wang, "On the full-range β dependence of ion-scale spectral break in the solar wind turbulence", The Astrophysical Journal **857**, 136 (2018).

[5] A. N. Kolmogorov, V. Levin, J. C. R. Hunt, O. M. Phillips, and D. Williams, "The local structure of turbulence in incompressible viscous fluid for very large reynolds numbers", Proceedings of the Royal Society of London. Series A: Mathematical and Physical Sciences **434**, 9–13 (1991).

[6] R. H. Kraichnan, "Inertial-range spectrum of hydromagnetic turbulence", The Physics of Fluids **8**, 1385–1387 (1965).

[7] J. W. Belcher and L. Davis Jr., "Large-amplitude alfvén waves in the interplanetary medium, 2", Journal of Geophysical Research (1896-1977) **76**, 3534–3563.

[8] J. V. Shebalin, W. H. Matthaeus, and D. Montgomery, "Anisotropy in mhd turbulence due to a mean magnetic field", Journal of Plasma Physics **29**, 525–547 (1983).

[9] S. Oughton, E. R. Priest, and W. H. Matthaeus, "The influence of a mean magnetic field on three-dimensional magnetohydrodynamic turbulence", Journal of Fluid Mechanics **280**, 95–117 (1994).

[10] P. Goldreich and S. Sridhar, "Toward a theory of interstellar turbulence. 2: Strong alfvenic turbulence", Astrophysical Journal **438**, 763–775 (1995).

[11] J. Maron and P. Goldreich, "Simulations of incompressible magnetohydrodynamic turbulence", The Astrophysical Journal **554**, 1175–1196 (2001).

[12]W.-C. Müller, D. Biskamp, and R. Grappin, "Statistical anisotropy of magnetohydrodynamic turbulence", Phys. Rev. E **67**, 066302 (2003).

[13]S. Boldyrev, "On the spectrum of magnetohydrodynamic turbulence", The Astrophysical Journal **626**, L37–L40 (2005).

[14]D. Gro šelj, C. H. K. Chen, A. Mallet, R. Samtaney, K. Schneider, and F. Jenko, "Kinetic turbulence in astrophysical plasmas: waves and/or structures?", Phys. Rev. X **9**, 031037 (2019).

[15]M. Wan, W. H. Matthaeus, H. Karimabadi, V. Roytershteyn, M. Shay, P. Wu, W. Daughton, B. Loring, and S. C. Chapman, "Intermittent dissipation at kinetic scales in collisionless plasma turbulence", Phys. Rev. Lett. **109**, 195001 (2012).

[16]A. Chasapis, W. H. Matthaeus, T. N. Parashar, M. Wan, C. C. Haggerty, C. J. Pollock, B. L. Giles, W. R. Paterson, J. Dorelli, D. J. Gershman, R. B. Torbert, C. T. Russell, P.-A. Lindqvist, Y. Khotyaintsev, T. E. Moore, R. E. Ergun, and J. L. Burch, "In situ observation of intermittent dissipation at kinetic scales in the earth's magnetosheath", The Astrophysical Journal **856**, L19 (2018).

[17]J. Egedal, W. Daughton, and A. Le, "Large-scale electron acceleration by parallel electric fields during magnetic reconnection", Nature Physics **8**, 321–324 (2012).

[18]J. F. Drake, M. Swisdak, H. Che, and M. A. Shay, "Electron acceleration from contracting magnetic islands during reconnection", **443**, 553–556 (2006).

[19]S. A. Markovskii and B. J. Vasquez, "A Short-timescale Channel of Dissipation of the Strong Solar Wind Turbulence", **739**, 22, 22 (2011).

[20]J. M. TenBarge and G. G. Howes, "CURRENT SHEETS AND COLLISIONLESS DAMPING IN KINETIC PLASMA TURBULENCE", The Astrophysical Journal **771**, L27 (2013).

[21]V. Demchenko and A. Hussein, "Stochastic heating of electrons and ions in an isothermal plasma by hydrodynamic current instability", Nuclear Fusion **14**, 229–235 (1974).

[22]J. Büchner and w. Daughton, "Role of current-aligned instabilities in reconnection", Cambridge, 144–153 (2007).

[23]S. P. Gary, "Short-wavelength plasma turbulence and temperature anisotropy instabilities: recent computational progress", Philosophical Transactions of the Royal Society A: Mathematical, Physical and Engineering Sciences **373**, 20140149 (2015).

[24]L. Matteini, "Kinetic instabilities in the solar wind: a short review", AIP Conference Proceedings **1720**, 030003 (2016).

[25]P. W. Gingell, D. Burgess, and L. Matteini, "THE THREE-DIMENSIONAL EVOLUTION OF ION-SCALE CURRENT SHEETS: TEARING AND DRIFT-KINK INSTABILITIES IN THE PRESENCE OF PROTON TEMPERATURE ANISOTROPY", The Astrophysical Journal **802**, 4 (2015).

[26]V. Zhdankin, D. A. Uzdensky, J. C. Perez, and S. Boldyrev, "STATISTICAL ANALYSIS OF CURRENT SHEETS IN THREE-DIMENSIONAL MAGNETOHYDRODYNAMIC TURBULENCE", The Astrophysical Journal **771**, 124 (2013).

[27]J. Büchner, C. Dum, and M. Scholer, "Space plasma simulation", Lecture Notes on Physics, v.615 (2003), 138 (2003).

[28]T. B. Bagdonat, "Hybrid simulation of weak comets", PhD thesis (Dec. 2004).

[29]J. Müller, S. Simon, U. Motschmann, J. Schüle, K.-H. Glassmeier, and G. J. Pringle, "A.i.k.e.f.: adaptive hybrid model for space plasma simulations", Computer Physics Communications **182**, 946–966 (2011).

[30]K. Makwana, V. Zhdankin, H. Li, W. Daughton, and F. Cattaneo, "Energy dynamics and current sheet structure in fluid and kinetic simulations of decaying magnetohydrodynamic turbulence", Physics of Plasmas **22** (2014) 10.1063/1.4916492.

[31]L. Franci, S. S. Cerri, F. Califano, S. Landi, E. Papini, A. Verdini, L. Matteini, F. Jenko, and P. Hellinger, "Magnetic reconnection as a driver for a sub-ion-scale cascade in plasma turbulence", The Astrophysical Journal **850**, L16 (2017).

[32]E. Papini, L. Franci, S. Landi, A. Verdini, L. Matteini, and P. Hellinger, "Can hall magnetohydrodynamics explain plasma turbulence at sub-ion scales?", The Astrophysical Journal **870**, 52 (2019).

[33]N. Jain and J. Buechner, "Free energy sources in kinetic scale current sheets formed in collisionless plasma turbulence", in Egu general assembly conference abstracts, EGU General Assembly Conference Abstracts (May 2020), p. 21518.

[34]N. Jain and J. Büchner, "Effect of guide field on three-dimensional electron shear flow instabilities in electron current sheets", Journal of Plasma Physics **81**, 905810606, 905810606 (2015).

[35]N. Jain and A. S. Sharma, "Evolution of electron current sheets in collisionless magnetic reconnection", Physics of Plasmas **22**, 102110 (2015).

[36]T. N. Parashar and W. H. Matthaeus, "Propinquity of current and vortex structures: effects on collisionless plasma heating", The Astrophysical Journal **832**, 57 (2016).

[37]K. Bergstedt, H. Ji, J. Jara-Almonte, J. Yoo, R. E. Ergun, and L. .-.-J. Chen, *Statistical properties of magnetic structures and energy dissipation during turbulent reconnection in the earth's magnetotail*, 2020.